Supporting Information

Responses of Defect-Rich Zr-Based Metal-Organic Frameworks towards NH_3 Adsorption

Tatchamapan Yoskamtorn[1,#], Pu Zhao[1,#], Xin-Ping Wu[2,*], Kirsty Purchase[1], Fabio Orlandi[3], Pascal Manuel[3], James Taylor[3], Yiyang Li[1], Sarah Day[4], Lin Ye[1], Chiu C. Tang[4], Yufei Zhao[5], S.C. Edman Tsang[1,*]

[1]Wolfson Catalysis Centre, Department of Chemistry, University of Oxford, Oxford OX1 3QR, U.K.

[2]Key Laboratory for Advanced Materials, and Centre for Computational Chemistry and Research Institute of Industrial Catalysis, East China University of Science and Technology, 130 Meilong Road, Shanghai 200237, P.R. China

[3]ISIS Neutron and Muon Source, Rutherford Appleton Laboratory, Didcot OX11 0QX, U.K.

[4]Diamond Light Source Ltd., Harwell Science and Innovation Campus, Didcot OX11 0DE, U.K.

[5]State Key Laboratory of Chemical Resource Engineering, Beijing University of Chemical Technology, Beijing, 100029, P.R. China

#These authors contributed equally.

*Email: edman.tsang@chem.ox.ac.uk (S. C. E. Tsang); xpwu@ecust.edu.cn (X.-P. Wu)

1) Experimental

A. Chemicals

All chemicals and solvents in this work were commercially available (Sigma-Aldrich and Fluorochem), with 98 % purity or above, and used as received.

B. Sample preparation

UiO-67 was prepared according to a procedure reported by J. F. Cavka *et al.* with some modifications.[1] 8 mL of *N,N*-dimethylformamide (DMF) was added into a glass vial containing 49 mg of Zirconium tetrachloride ($ZrCl_4$), 378 mg of glacial acetic acid, and 52 mg of biphenyl-*4,4′*-dicarboxylic acid (H_2BPDC). The mixture was homogenised via sonication for 10 min, followed by solvothermal treatment at 393 K for 24 h. The solid product was washed with DMF three times, methanol three times, followed by methanol exchange for three days. During this period, methanol was exchanged daily. The final product was collected by centrifugation and activated at 423 K under vacuum for 12 h before storing in a desiccator. Anal. Calcd for $Zr_6O_{32}H_{48}C_{64}$ (i.e. $Zr_6O_4(OH)_4(bpdc)_{6-x}(acetate)_{2x}$ where x= 2.0): C/Zr, 1.40. Found: C/Zr, 1.41± 0.5.

UiO-bpydc was prepared by using the procedure similar to UiO-67, except 52 mg of *2,2′*-bipyridine-*5,5′*-dicarboxylic acid (H_2BPYDC) was used instead of H_2BPDC. Anal. Calcd for $Zr_6O_{32}H_{40}C_{60}N_9$ (i.e. $Zr_6O_4(OH)_4(bpydc)_{6-x}(acetate)_{2x}$ where x= 1.5): C/Zr, 1.32. Found: C/Zr, 1.31± 0.5.

Healed UiO-67 and UiO-bpydc were synthesised according to the procedure published by O. V. Gutov *et al.* with some modifications.[2] 100 mg of each sample and 60 mg of its corresponding linker were dispersed in a vial containing 10 ml DMF solution. The mixture vial was sealed securely and sonicated for 15 minutes before placing in an oven at 393 K for 48 h. The precipitate was separated from the suspension by centrifugation and intensively washed five times with hot DMF and four times with methanol, followed by methanol exchange for three days. The final product was evacuated with gradual heating to 423 K for 12 h and kept in a desiccator. Anal. Calcd for healed UiO-67 $Zr_6O_{32}H_{52}C_{84}$ (i.e. $Zr_6O_4(OH)_4(bpdc)_{6-x}(acetate)_{2x}$ where x= 0.0): C/Zr, 1.84. Found: C/Zr, 1.83± 0.5. Anal. Calcd for healed UiO-bpydc $Zr_6O_{32}H_{40}C_{65.6}N_{10.4}$ (i.e. $Zr_6O_4(OH)_4(bpydc)_{6-x}(acetate)_{2x}$ where x= 0.8): C/Zr, 1.44. Found: C/Zr, 1.43± 0.5.

C. Characterisation techniques

X-ray powder diffraction (XRD): Laboratory XRD was performed by using a Bruker D8 Advance X-ray diffractometer operated at 40 kV and 40 mA with Cu $K_{\alpha 1}$ radiation (λ = 1.54056 Å).

Thermogravimetric analysis (TGA): TGA was performed on a TA Instruments TGA Q600 under an airflow of 100 ml/min. A sample with an exact amount (10-15 mg) was added into an alumina pan and heated from room temperature to 1173 K using the heating rate of 10 K/min. A corresponding TGA curve together with its first derivative was collected simultaneously.

Elemental analysis: C H N elemental analysis was acquired on a LECO brand CHNS-932 Analyzer. Quantity of Zr in an acid-digested sample was confirmed by inductively coupled plasma mass spectrometry (ICP-MS) with an Agilent 7800 ICP-MS instrument.

^{1}H Nuclear magnetic resonance (NMR) of digested samples: Prior to the ^{1}H NMR measurement, sample digestion was conducted as follows: 1 mL of 0.1 M NaOH in D_2O was placed into a glass vial containing 10 mg of a MOF sample. The mixture was sonicated for 5 min and left overnight to allow complete decomposition of the MOF framework, i.e. Zr oxoclusters are precipitated out as Zirconium oxides (ZrO_2) and the other components such as organic linkers and capping species are entirely dissolved in the basic solution. NMR spectra of the digested MOF solution were recorded on a Bruker AVIIIHD 400 nanobay NMR spectrometer.

N_2 physisorption: N_2 adsorption isotherm measured at 77 K and up to 1 bar was recorded on a Micromeritics Tristar instrument. All sorption isotherms were obtained using ultrahigh purity gases (99.999%). Before the sorption analysis, a sample (0.1−0.2 g) was loaded into a sample cell and subjected to a vacuum of 10^{-5} Torr at 423 K for 12 h. N_2 adsorption data with an initial slope (0.01 to 0.1 P/P_0) permitted calculation of the apparent surface areas based on the Brunauer-Emmett-Teller (BET) equations. Pore size distribution (PSD) was calculated by DFT embedded in a Micromeritics software. A model used in the PSD analysis is based on a slit-type pore structure with carbon surface analysed by N_2 at 77 K.

NH_3 temperature-programmed desorption (NH_3-TPD): NH_3-TPD spectrum was measured with a Micromeritics AutoChem II 2910 apparatus. The detection of desorbed molecules was done by the thermal conductivity detector. About 100 mg of sample was degassed in a quartz cell at 573 K for 1 h, exposed to NH_3 which was used as a probe molecule at 373 K for 30 min, and then evacuated at 373 K for 15 min by purging with helium. TPD measurement was done from room temperature to 593 K with a heating rate of 10 K/min and with helium as carrier gas having a flow rate of 40 cm^3/min.

Volumetric analysis: NH_3 sorption isotherms of the samples were carried out by using a gas adsorption analyser (Quantachrome Autosorb iQ-Chemi). Each sample was placed in a chamber and outgassed under vacuum at 423 K for 24 h before testing. 99.9% NH_3 gas was loaded into the sample chamber at 298 K with a loading of 5 cm^3/time from 0 up to 1100 mbar.

Gravimetric analysis by IGA: The Intelligent Gravimetric Analyser (IGA-001, Hiden) was employed to measure the cycling stability of MOF samples upon NH_3 uptake. The NH_3 gas used is 99.999 % purity, CK Gas Company. Prior to the measurement, a sample in a vessel of IGA was degassed under 10^{-5} Pa at 423 K for 8 h. A built-in water bath was used to keep the temperature isothermally at 298 K. NH_3 was dosed to the sample at a maximum rate from 0 to 600 mbar. Then, the sample was evacuated at 298 K for 1 h and heated at 423 K until the sample weight stabilized. The sample was cooled down to 298 K again before repeating the cycle test for three times.

***In-situ* neutron powder diffraction (*In-situ* NPD)** for ammonia adsorption: An *in-situ* NPD at WISH instrument[3] was used to study the binding sites of NH_3 (ND_3, 99 %) and the structural change of the Zr-based MOFs as a function of increased ND_3 loading. This structural information was achieved by the use of Rietveld refinement. Prior to the measurement, a sample was loaded into an 11 mm diameter vanadium can with quartz wool on top. The sample was degassed under high vacuum at 373 K (5 K/min heating rate) for 24 h to remove any guest molecules and then naturally cooled down to room temperature. The sample holder was transferred to a vacuum chamber connected to a gas handling system. An NPD pattern of the desolvated sample was first collected at 300 K for 20 min. After that, a He cryostat was used to cool down the sample can to 7 K, where the thermal motion of the MOF sample and adsorbed ND_3 molecules can be significantly reduced. High-resolution NPD of this sample was carried out for 1 hour to get good statistics. After the measurement, the sample was gently heated up to 300 K before dosing with ND_3 gas by using a calibrated volume. Each of the loading steps required half an hour to enable the homogenous dispersion of ND_3 molecules inside the crystalline sample. NPD patterns after each ND_3 loading were measured at 300 K and 7 K for 20 min and 1 h, respectively. Prior to the low-temperature data collection at 7 K, the system was cooled down to 7 K slowly over 3 h in order to eliminate the gas condensation outside the sample. The gas handling system and sample environment at WISH are demonstrated in Figure S1.

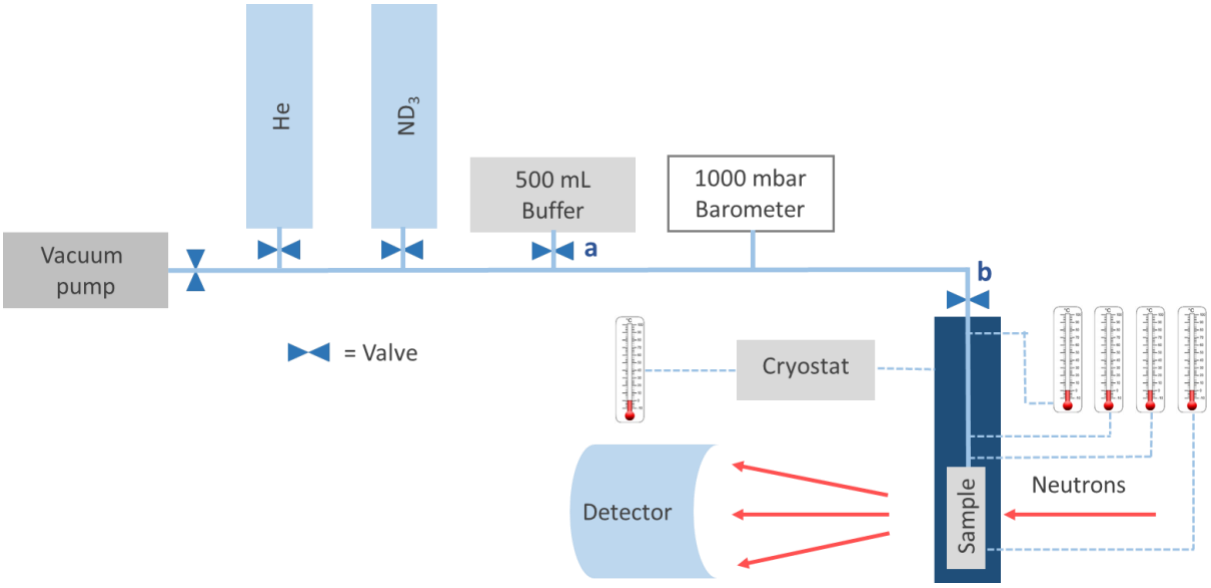

Figure S1 | Schematic diagram of the neutron diffraction set up at WISH beamline, ISIS.

Volume calibration along with ND_3 dosing was performed at 298 K by using the procedure adopted from the literature[4]. Helium (He) was used as a calibration gas. According to Figure S1, a certain pressure of He (P_a) was loaded into a known volume (V_a) of a 500 mL buffer while keeping the other parts evacuated. An actual volume of the system excluding the sample stick and the sample cell (V_b, to the valve b) was then calculated by using a final pressure of He (P_b) after closing a vacuum valve and opening a buffer valve to reach the V_b volume. From the ideal gas law, we can achieve the value of V_b:

$$V_b = \frac{V_a P_a}{P_b} \qquad \text{Supplementary Equation (1)}$$

The same procedure was also applied to determine an actual volume of the whole system including the sample stick and the sample cell (V_c). Assuming that the He adsorption capacity of UiO-67 and UiO-bpydc is negligible at 298 K,[5] V_c is then the total volume of the system. After the volume calibration, the sample together with the rest of the gas handling system was evacuated to 10^{-5} Pa for 1 h to completely remove the He gas. The valve b was closed prior to dosing the ND_3 gas into the system with a set pressure of P_2. The initial amount of ND_3 in the system (n_2) can be derived from the following equation:

$$P_2V_b = n_2RT \qquad \text{Supplementary Equation (2)}$$

where R and T are the ideal gas constant and the temperature, respectively.

When the valve b is open to allow ND_3 adsorption into the sample, the final ND_3 pressure will stabilize at P_3. Then we can get the amount of residual ND_3 left in the system (n_3):

$$P_3V_c = n_3RT \qquad \text{Supplementary Equation (3)}$$

The actual amount of ND_3 adsorbed (n) by the sample is then calculated:

$$n = n_2 - n_3 \qquad \text{Supplementary Equation (4)}$$

The precise dosing amount of ND_3 in a unit of mmol/g can be obtained since we know the weight of the sample used.

In the temperature-dependent study by *in situ* NPD, it is essential to keep the same ND_3 quantity in the internal pores of the powder sample as close as possible. As shown in the set up above (based on the similar BET/Chemisorption equipment and procedure), the sample was first placed in the sample tube with repeated flushing and evacuation. We then loaded pure ND_3 stepwise through opening the valve b. Notice that the dosing volume (deliver volume up to valve b) and the volume in the sample tube with the sample (between valve b to the sample bottom) were carefully pre-calibrated with inert gas. As a result, the total desired gas loading to the sample can be precisely worked out from the pressure transducers (pressure differences) before dosage and after equilibration for the subsequent dosing at different pressures before saturation. Given the high surface area of the powder MOF sample (at high loading) compared to the small top gas volume and the closure of the valve b, the data collection at room temperature (298 K) was first collected. Following on this, the cooling process was taken until at 7 K with the valve b remained closed.

One may doubt that under equilibrium conditions the ND_3 adsorbed quantity of the MOF sample must change when decreasing the temperature as a result of the reduced kinetic energy of the adsorbates, considering the dead volume of the sample cell. However, the MOF has much high surface area for gas uptake than residue gas of the dead volume and our loading procedure can minimise the ND_3 variation in the sample at different temperatures as the follows:

I) A calibrated pressure of ND_3 was loaded into the known volume of the 500 mL buffer and the other part up to valve b (see Figure S1). After the pressure was stabilised, valve b was opened to allow ND_3 to be adsorbed in the pre-evacuated sample. After the ND_3 pressure reached the target pressure, valve b was immediately closed to prevent more ND_3 molecules from entering the sample stick and vessel. This means the sample stick and vessel were isolated and sealed before achieving equilibrium. At this point, free gaseous ND_3 molecules above the sample up to valve b can be continuously adsorbed into the sample and hence leaving a negligible amount of gas residues in a gas phase. This is based on the fact that the UiO-67-type MOFs exhibit NH_3 uptake as high as 8.4 mmol/g at 298 K and 1100 mbar of pure NH_3 gas.

II) The actual dead volume of the sample vessel up to valve b is approximately 16.5 cm^3, whilst the actual volumes of UiO-67 and UiO-bpydc are 2.43 and 2.14 cm^3, respectively. The known dead volume can be used to determine the maximum ND_3 residues outside the sample. In the worst scenario where no more ND_3 molecules are further adsorbed into the sample after closing the valve b, the molar ratio of the unadsorbed ND_3 to the adsorbed ND_3 in the UiO- 67 sample is less than 5.24 % at the highest loading and becomes lower at the lower dosage (4.55 and 4.03 % at the second and the first ND_3 loadings, respectively). In addition, based on point I, after closing valve b, more ND_3 molecules are further adsorbed into the sample. Therefore, the molar ratio of the unadsorbed ND_3 to the adsorbed ND_3 should be even smaller. Thus, we are confident that the effect of the dead volume is not significant in our gas loading system and the change in adsorbed quantity at different temperatures can be negligible. Such a small amount of unadsorbed ND_3 at room temperature will not change the MOF structures and the diffraction data significantly upon cooling. In addition, there have been some studies in the literature related to MOFs gas adsorptions, which used similar gas-handling systems [4, 6-8]

To assure there is no major change in gas uptake value in the sample, we compared the total ND_3 occupancies derived from the Rietveld refinement of neutron powder diffraction (NPD) data at different temperatures (see Table S16). The results clearly demonstrate that no significant alteration in the total ND_3 occupancies is observed, endorsing that change in the adsorbed amount of ND_3 at different temperatures is negligible in our experiment setup.

Synchrotron powder X-ray diffraction (SXRD): SXRD data were collected on Beamline I11[9], Diamond Light Source, UK. The energy of the incident X-ray flux was set at 15 keV. The wavelength and the 2θ-zero point were refined using a diffraction pattern obtained from a high-quality silicon powder (SRM640c). For the gas-free samples, each sample powder was ground and loaded in a 0.5 mm borosilicate glass capillary and then activated under vacuum at 423 K for 2 h. For the NH_3-loaded samples, each sample was degassed at 473 K for 3 h under reduced pressure using a Schlenk line. The sample was then naturally cooled down to the room temperature and exposed to an NH_3 vapour for 30 min. The sample was loaded into a quartz-type capillary with a diameter of 0.5 mm and sealed perfectly by using a flame. High-resolution SXRD data of all samples were achieved by using the multi-analyser crystals (MAC) detectors in the 2θ range 0-150° with 0.001° data binning. Each MAC pattern was collected for an hour to get satisfying statistics.

***In-situ* synchrotron powder X-ray diffraction (*In-situ* SXRD) for ammonia desorption**: *In-situ* SXRD pattern of the NH_3-loaded UiO-bpydc (NH_3@Uio-bpydc) was collected at Beamline BL02B2, Spring 8, Japan. The energy of the incident X-ray flux was set at 37 keV. The wavelength and the 2θ-zero point were refined using a diffraction pattern obtained from a Si (1 1 1) double-crystal monochromator. High-resolution SXRD data of all samples were achieved by using the position-sensitive detectors (PSDs) in the 2θ range 2-80° with 0.001° data binning. The capillary was mounted to a sample holder and heated up from room temperature to 773 K with a ramping rate of 5 K/min. Each PSD pattern was collected every 2 K of increasing temperature with a scanning time of 2 s. At 373, 473, 573, 673 and 773 K, The diffraction patterns were scanned by using a time per step of 120 s for good statistics.

***In-situ* inelastic neutron scattering (INS) experiment.** TOSCA[10] instrument, an INS spectrometer with an indirect time-of-flight (TOF) geometry at the ISIS Pulsed Neutron and Muon Source, Rutherford Appleton Laboratory, was used to study the dynamic interactions between stored NH_3 (99.9%) and the host structures of UiO-67 and UiO-bpydc, as a function of increased NH_3 loading. The TOSCA has a wide energy transfer range of 0- 4000 cm^{-1} (0- 500 meV) and a high resolution of 1.5% $\Delta E/E$ with the best results below 2000 cm^{-1} (250 meV). A pulsed polychromatic beam of neutrons hit a sample at a certain flight path of 17 m from the source. The neutrons inelastically scattered by the sample were then reflected by a pyrolytic graphite *(002)* analyser combined with a cooled Be filter to give a unique final energy of ~32 cm^{-1}. The fixed energy neutrons finally travelled towards ten detector banks each having thirteen ^3He tubes. Five banks are located in forward scattering and the other five in backward scattering geometries with scattered angles of 45 ° and 135 °, respectively. Thanks to the low final energy, a relationship between energy transfer (E_T, cm^{-1}) and momentum transfer (Q, $Å^{-1}$) are directly translated to $E_T \approx 16Q^2$. The TOF data were converted to the dynamic structure factor, S(Q,ω), and rebinned in energy transfer by using the Mantid software developed at ISIS.[11] Prior to the measurement, a sample (1.0-1.5 g) was loaded into a 11 mm diameter vanadium can with quartz wool on top and sealed with an Indium wire. The sample was degassed under high vacuum at 373 K (5 K/min

heating rate) for 24 h to remove any guest molecules and then naturally cooled down to room temperature. The sample can was mounted at the end of the stick and connected to a gas handling and a temperature control system. Leak check was done before cooling down the sample can to below 10 ± 0.1 K within a closed cycle refrigerator (CCR) cryostat, where the thermal motion of the MOF sample and adsorbed NH_3 molecules can be significantly reduced. An INS spectrum of the desolvated sample was carried out for at least 4 hours for a good statistics. After the measurement, the sample was gently heated up to 300 K before dosing with NH_3 gas at the desired amount by using a calibrated volume. Each of the loading step required half an hour to enable homogeneous dispersion of NH_3 molecules inside the crystalline sample. The INS spectrum of each ammoniated sample was measured below 10 K similar to its pristine sample. The signal of the background from the instrument and the vanadium sample holder was subtracted from the INS spectra of the samples. The gas handling system and sample environment at TOSCA are similar to one at WISH beamline, except gaseous ND_3 was replaced by NH_3.

D) Data analysis

Rietveld refinement of gas-free samples: TOPAS-academic 5 software[12], containing Rietveld refinement methods, was used to analyse the structural information of the diffraction patterns. For structural refinement, the initial MOF models were based on crystallographic data of UiO-67[13], and UiO-bpydc[14]. The diffraction patterns were refined by optimisation of the scale factor and lattice parameters. The background was described by a shifted Chebyschev function. A back-to-back exponential convoluted with pseuduo-voigt peakshape function was used to describe the peak asymmetry in the time-of-flight (tof) data. Both biphenyl-*4,4′*-dicarboxylate (bpdc) and *2,2′*-bipyridine-*5,5′*-dicarboxylate (bpydc) linkers were treated as rigid bodies using Cartesian coordinates to reduce the number of variables. Dummy atoms were added to define the origins of the rigid bodies. The refined structural parameters for all atoms of each pattern were the coordinates (x, y, z) and isotropic displacement factors (B_{eq}). The quality of the Rietveld refinements of diffraction data was confirmed by low values of goodness-of-fit (GOF, χ^2) and *R* factors (R_{wp}, R_p, R_{exp}) and a well fitted pattern with acceptable B_{eq} within experimental errors. All the errors of the atom−atom distances were calculated using the following equation:

$$r_{\text{error}}=\sqrt{(x_{\text{error}})^2+(y_{\text{error}})^2+(z_{\text{error}})^2}\times r_{\text{measure}} \qquad \text{Supplementary Equation (5)}$$

where r_{error} is the error of the measured atom−atom distance, x_{error}, y_{error}, z_{error} are the errors of the fractional coordinates (x, y, z) respectively, r_{measure} is the measured atom−atom distance.

Rietveld refinement of ND_3-loaded samples: For the ammoniated samples, the possible locations of ND_3 molecules inside the MOF cavities were determined by using a Fourier difference map, generated in the TOPAS-5 software. The structures of the guest-free UiO-67 and UiO-bpydc were used as starting models with constant occupancies and isotropic displacement factors. Thanks to the porous structure and chemical properties of the MOFs, interacting ND_3 molecules with a dynamic size of 2.5 Å were expected to adsorb inside the pore, on the basal planes of linkers, and close to metal nodes. Each ND_3 molecule was treated as a rigid body described by Z-matrix with N–H bond distance and H–N–H bond angle constrained in the range of 1.04-1.07 Å and 106.0-107.0°, respectively. The ND_3 molecule was added into the MOF structure one by one. Coordinates and site occupancy of the ND_3 molecule were freely refined. Fitting parameters including *Gof* and

R factors, were used to prove the quality of the refinement. The lower values of these factors, the more accurate refinement close to the real structure.

Neutron diffraction: Rietveld refinement was performed over the diffraction data recorded on the average 2θ = 58.3 ° detector bank.

Synchrotron diffraction: Rietveld refinement was performed over the whole data range (2θ = 5−40 °).

CCDC 2047200, 2047201, 2047202, 2047203, 2047204, and 2047205 contain the supplementary crystallographic data for this paper. The data can be obtained free of charge from The Cambridge Crystallographic Data Centre via www.ccdc.cam.ac.uk/structures. A list of the crystal structures obtained from the Rietveld refinements of the NPD data at 300 K and their corresponding CCDC Deposition numbers is given below;

CCDC 2047200: UiO-67 with the first ND_3 loading

CCDC 2047201: UiO-67 with the third ND_3 loading

CCDC 2047202: UiO-bpydc with the first ND_3 loading

CCDC 2047203: UiO-bpydc with the second ND_3 loading

CCDC 2047204: UiO-bpydc with the third ND_3 loading

CCDC 2047205: UiO-67 with the second ND_3 loading

E) Density Functional Theory (DFT) calculations

Calculations of binding energies: The valence-core interactions were described by using the projector-augmented wave (PAW) method[15] at a kinetic energy cutoff of 500 eV. The 2×2×2 *k*-point mesh was used for Brillouin zone integrations. For geometry optimisations, we used a Hellman−Feynman force criterion of 0.02 eV/Å on each ion.

Binding energy per NH_3 molecule (E_b) of a MOF-$n$$NH_3$ system was calculated as follows:

$$E_b = \frac{1}{n}\{E[\mathrm{MOF}] + nE[\mathrm{NH_3}] - E[\mathrm{MOF}-n\mathrm{NH_3}]\}, \quad \text{Supplementary Equation (6)}$$

where n is the number of NH_3 molecules in the MOF-$n$$NH_3$ system and $E[\mathrm{MOF}]$, $E[\mathrm{NH_3}]$, and $E[\mathrm{MOF}-n\mathrm{NH_3}]$ are the DFT calculated energies of the bare MOF, NH_3 molecule, and MOF-$n$$NH_3$ system, respectively.

Due to the large size of the MOF systems, we were not able to include dispersion corrections (e.g., the DFT-D3 scheme[16] of Grimme) in our DFT calculations because dispersion-corrected DFT calculations require much larger memory in computations than normal DFT calculations. Although the binding energies obtained from normal DFT calculations are underestimated, the differences of binding energies from normal DFT calculations are expected to be similar to that from dispersion-corrected DFT calculations.

Calculations of rotational energy barriers: The rotational energy barriers of NH_3-free and NH_3-loaded UiO-67 and UiO-bpydc were estimated by calculations on cluster models using M06-2X[17] functional with the def2-TZVP[18-19] basis set. Specifically, we considered four cases, namely the

guest-free UiO-67, UiO-67-1NH_3, guest-free UiO-bpydc, and UiO-bpydc-1NH_3; the corresponding cluster models are proton-capped bpdc, bpdc-1NH_3, bpydc, and bpydc-1NH_3 which were cut from the optimised periodic structures. The rotational groups (dihedral angle O1-C1-C2-C3, see Figure S45) were rotated between γ (i.e., the dihedral angle O1-C1-C2-C3 of the most stable configuration) and γ+180° (half a period) with 10° increments to scan the potential energy surfaces. During the scan, only the dihedral angle and the COO groups were fixed. The rotation energy barriers were computed as the energy difference between the most unstable and the most stable configurations (Table S16). These cluster calculations were carried out with the *Gaussian 16* program.[20]

2. Supplementary results

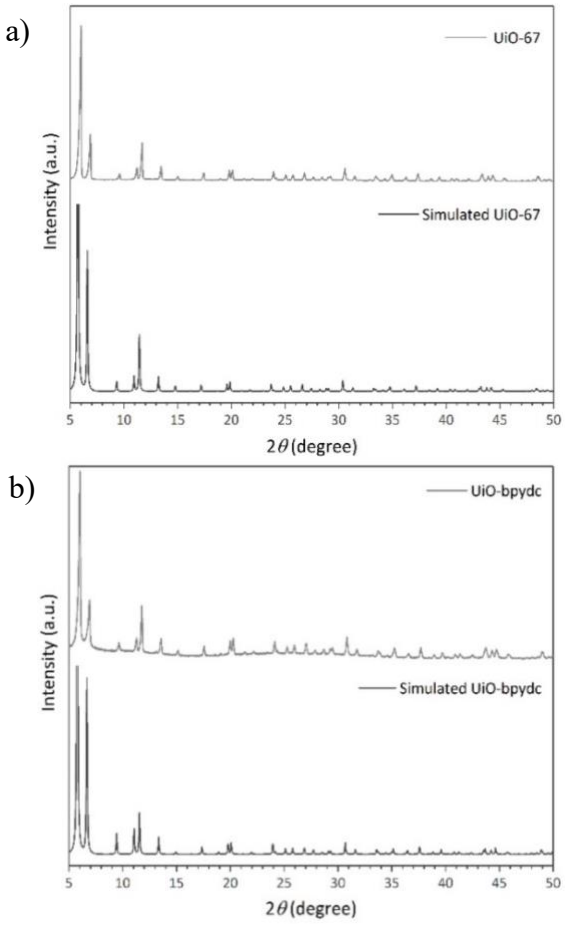

Figure S2 | Powder XRD patterns of UiO-67 (a) and UiO-bpydc (b) along with their corresponding diffraction patterns obtained from the literature.[1, 13] Note that the simulated patterns are derived from single-crystal diffraction data of the solvated samples. Thus, inclusion of the disordered solvent molecules such as water or *N,N*-dimethylformamide in the crystals as well as structural defects in powdered samples could cause the differences in peak intensities compared to the observed diffraction patterns.

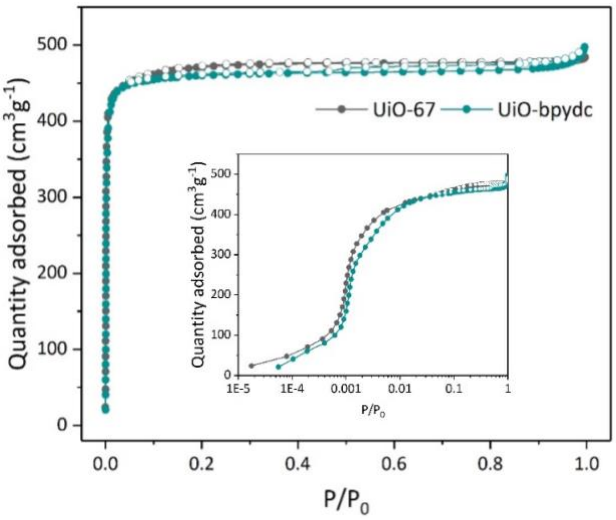

Figure S3 | N_2 physisorption isotherms of activated samples at 77 K. The isotherms indicate the typical microporous structures. Inset is the isotherms plotted in semi-log scale at low relative pressure. The isotherms of UiO-67 and UiO-bpydc show a slight step at ca. 0.1 P/P_o due to the presence of two types of pore windows. BET specific surface area and pore volume of UiO-67 and UiO-bpydc are 1916 m^2/g, 0.75 cm^3/g and 1953 m^2/g, 0.76 cm^3/g, respectively.

Table S1 | Corresponding missing linkers of the MOF samples derived from the elemental analyses and ICP-MS techniques.

Sample	Numbers of missing linker (x) per formula unit	Actual formula $Zr_6O_4(OH)_4(bpdc)_{6-x}(acetate)_{2x}$
UiO-67	2.0 ± 0.5	$Zr_6O_4(OH)_4(bpdc)_4(acetate)_4$
UiO-67-healed	0.0± 0.5	$Zr_6O_4(OH)_4(bpdc)_6$
UiO-bpydc	1.5 ± 0.5	$Zr_6O_4(OH)_4(bpydc)_{4.5}(acetate)_3$
UiO-bpydc-healed	0.8 ± 0.5	$Zr_6O_4(OH)_4(bpydc)_{5.2}(acetate)_{1.6}$

Note: Six linkers per formula unit is equivalent to twelve linkers coordinated to each metal node. The analysed samples were from different batches with respect to those used in the TGA experiments.

Table S2 | Corresponding missing linkers of the MOF samples obtained from the TGA results.

Sample	Weight loss (%) between 350 and 600 °C	Numbers of missing linker (x) per formula unit	Actual formula $Zr_6O_4(OH)_4(bpdc)_{6-x}(acetate)_{2x}$
UiO-bpydc	61.2	1.8 ± 0.3	$Zr_6O_4(OH)_4(bpydc)_{4.2}(acetate)_{3.6}$
UiO-bpydc-healed	63.3	1.4 ± 0.3	$Zr_6O_4(OH)_4(bpydc)_{4.6}(acetate)_{2.8}$

Note: Six linkers per formula unit is equivalent to twelve linkers coordinated to each metal node.

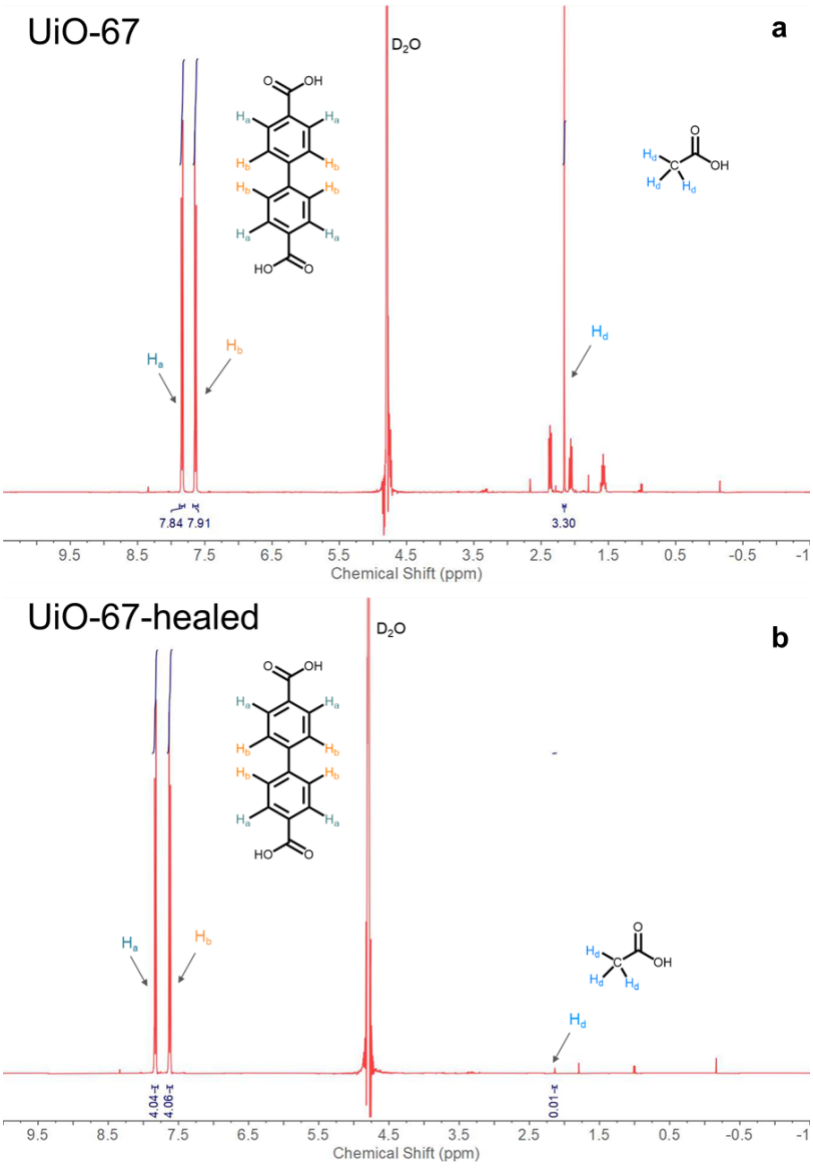

Figure S4 | ^{1}H NMR spectra of aliquots from the UiO-67 (**a**) and UiO-67-healed (**b**) in 0.1 M NaOH in D_2O at 298 K. The chemical shift of H_2bpdc linker: δ 7.88 – 7.79 (m, 4H), 7.66 – 7.58 (m, 4H) and acetic acid: *δ* 2.16 (s, 3H).

The above ^{1}H NMR results reveal the presence of acetic acid in the unhealed sample (**a**) indicating that missing linker defects are feasibly terminated by acetates. After the healing process (**b**), the signal from acetic acid almost disappears implying the completion of linker exchange with H_2bpdc.

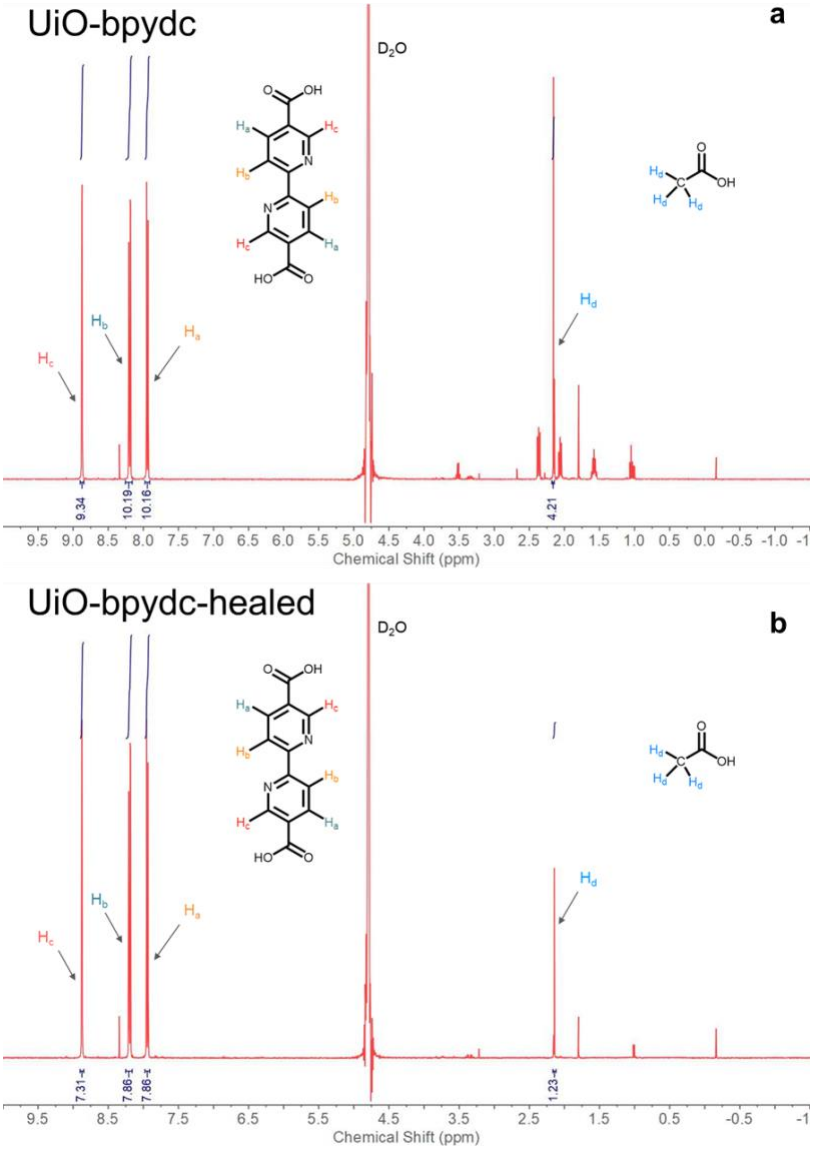

Figure S5 | ^{1}H NMR spectra of aliquots from the UiO-bpydc (**a**) and UiO-bpydc-healed (**b**) in 0.1 M NaOH in D_2O at 298 K. The chemical shift of H_2bpydc linker: δ 8.87 (dd, 2H), 8.20 (dd, 2H), 7.94 (dd, 2H) and acetic acid: *δ* 2.16 (s, 3H).

The above ^{1}H NMR results show the presence of acetic acid in the unhealed sample (**a**) indicating that missing linker defects are feasibly terminated by acetates. After the healing treatment (**b**), a drastic decrease of the signal from acetic acid is observed suggesting that most of the defect capping acetates are substituted by H_2bpydc linkers.

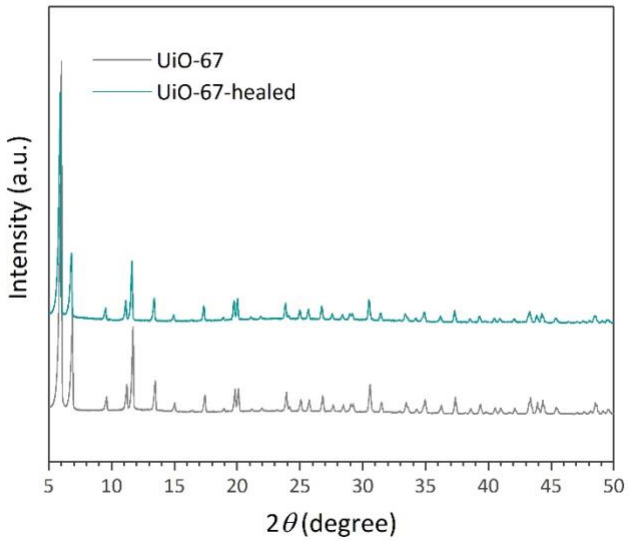

Figure S6 | Powder XRD patterns of UiO-67 samples before and after the healing process.

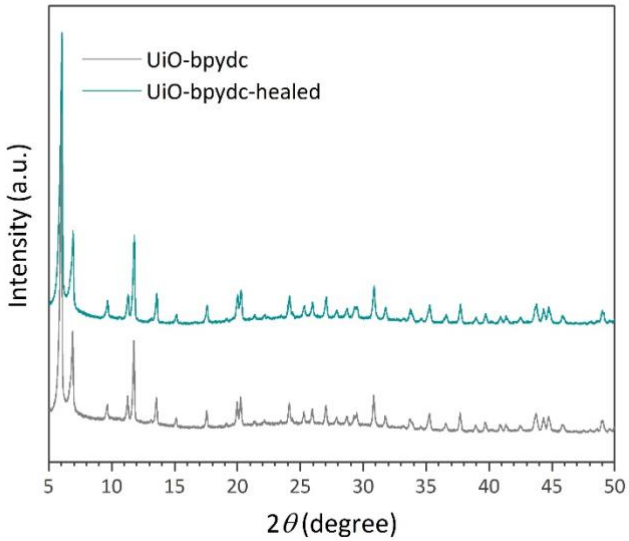

Figure S7 | Powder XRD patterns of UiO-bpydc samples before and after the healing process.

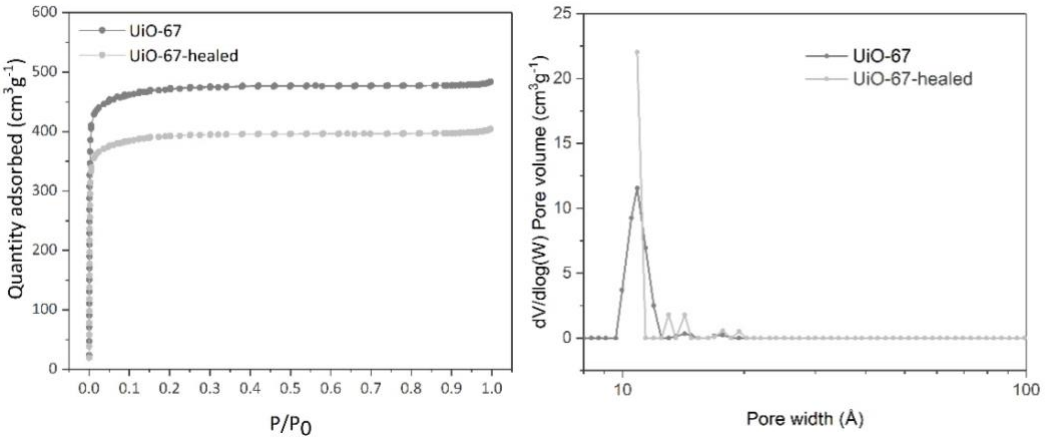

Figure S8 | N_2 sorption profiles and pore size distribution of UiO-67 samples before and after the healing process. The BET specific surface area and pore volume are changed from 1916 m^2/g, 0.75 cm^3/g to 1961 m^2/g, 0.72 cm^3/g, respectively. Pore size distribution (PSD) was examined by DFT embedded in a Micromeritics software. A model used in the PSD analysis is based on a slit-type pore structure with carbon surface.

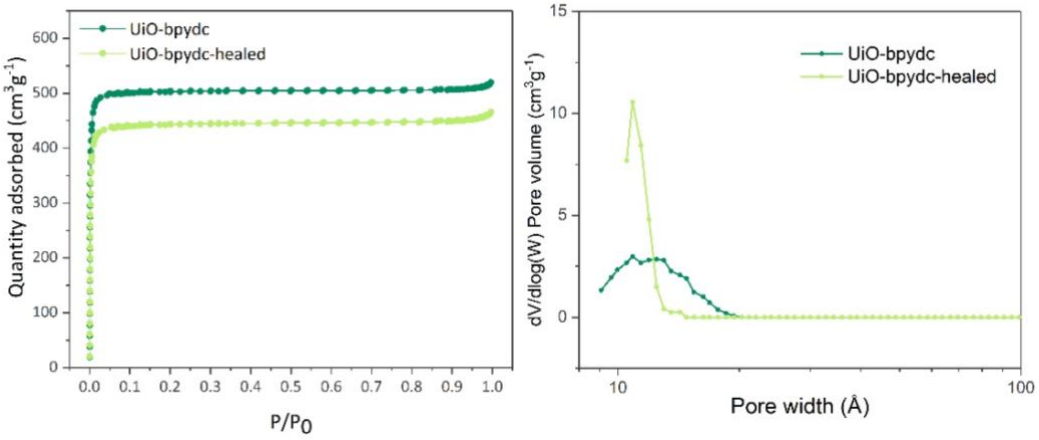

Figure S9 | N_2 sorption profiles and pore size distribution of UiO-bpydc samples before and after the healing process. The BET specific surface area and pore volume are changed from 1953 m^2/g, 0.76 cm^3/g to 1948 m^2/g, 0.72 cm^3/g, respectively. Pore size distribution (PSD) was examined by DFT method embedded in a Micromeritics software. A model used in the PSD analysis is based on a slit-type pore structure with carbon surface.

The non-uniform porous structure is due to the non-monodisperse pore structure created by missing linker defects as indicated by pore size distribution (PSD) analyses (see Figure S8 and S9). The defective MOF samples show broad PSD whereas their corresponding samples after the healing process (ligand exchange) have much smaller PSD centred at 11 Å. This result imply that the non-monodisperse pore structures of the defect-rich UiO-67 type MOFs in this work is caused by the missing linker defects. Similar PSD analyses of UiO-67 can be also found in https://pubs.acs.org/doi/full/10.1021/acsami.9b02764.

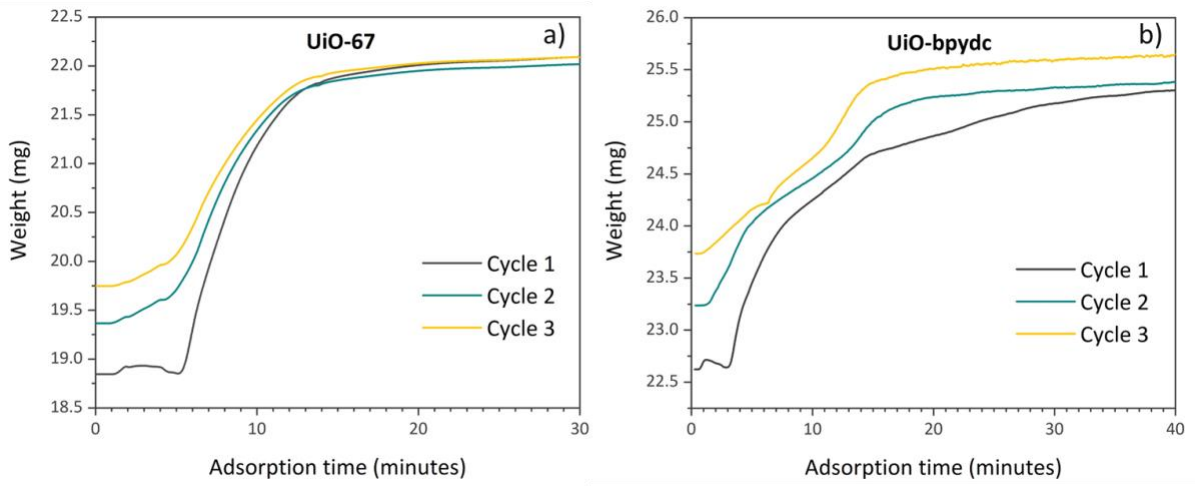

Figure S10 | Stability tests of UiO-67 (a) and UiO-bpydc (b) for NH_3 uptake, measured by repeated gravimetric analysis. The adsorption temperature and the maximum NH_3 pressure used were 298 K and 600 mbar, respectively.

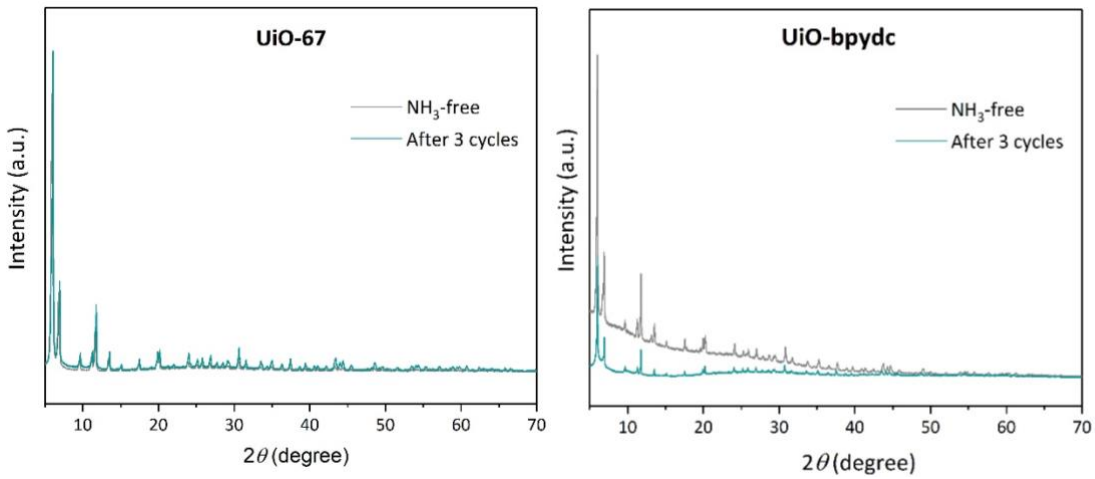

Figure S11 | Powder XRD patterns of defective Zr-based MOFs before and after three cycles of NH_3 adsorption at 298 K and up to 600 mbar of NH_3 pressure, measured by gravimetric analysis

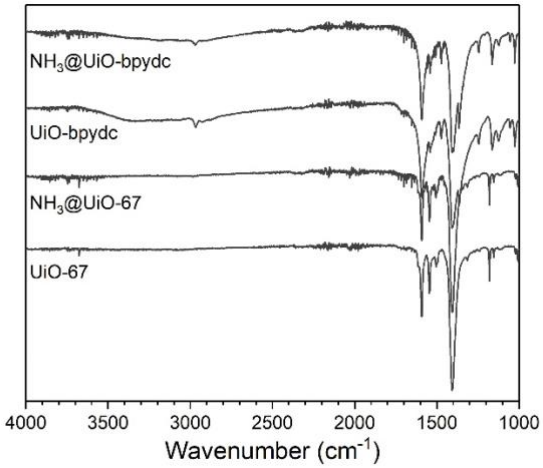

Figure S12 | FT-IR spectra of the samples before and after NH_3 adsorption at room temperature. Before the NH_3 adsorption each sample was placed in a bottom flask and activated at 423 K for 24 hrs under vacuum by using a Schlenk line. After being cooled to room temperature, the sample was exposed to NH_3 vapor for 30 mins, sealed tightly and kept in a dry place for one week.

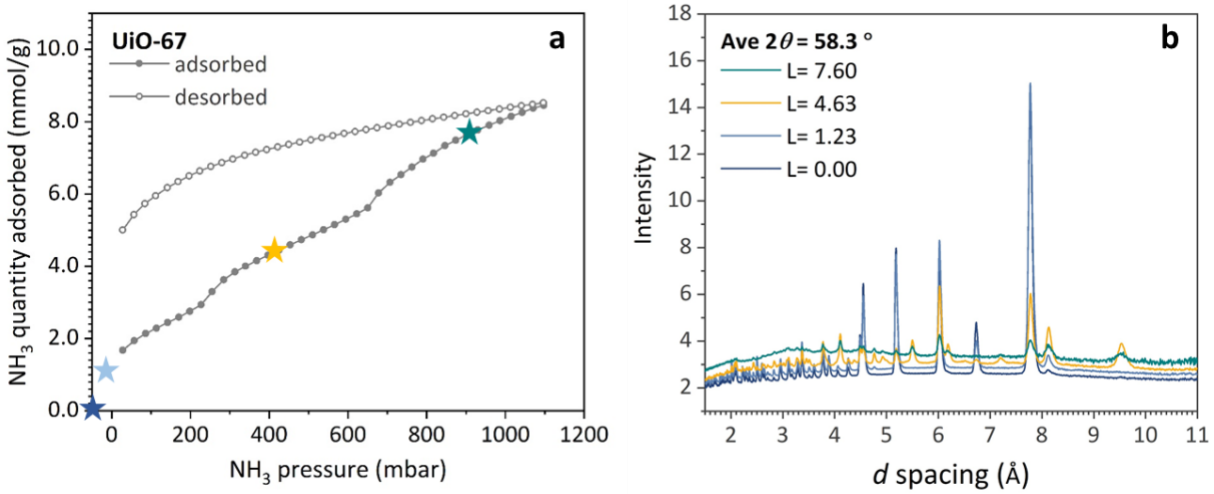

Figure S13 | *In situ* NPD patterns of defective UiO-67 at various loadings of ND_3: (a) Each dosing point was marked as a star symbol in the stepwise NH_3 adsorption isotherm measured at 298 K and up to 1100 mbar of NH_3 pressure; (b) corresponding NPD patterns collected at 300 K on the average 2θ = 58.3 ° detector bank. L refers to the dosing amount of ND_3 in mmol/g.

Under room temperature the open-ended desorption isotherm clearly indicates that some adsorbed NH_3 molecules partially retain in the MOF sample due to the strongly binding interaction (potentially at μ_3-OH sites). A more dramatic treatments including the uses of higher temperature and evacuation should be done to complete the desorption in a complete cycle.

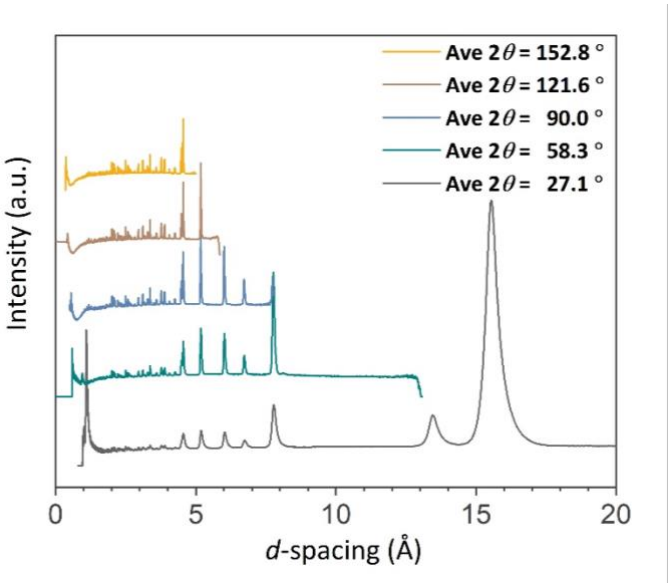

Figure S14 | ND patterns of ND_3-free UiO-67 recorded at 300 K by using different detector banks. Ave 2θ refers to the average 2θ of the detector banks.

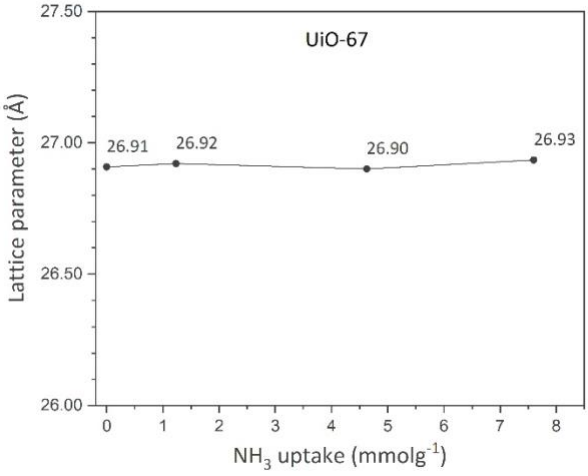

Figure S15 | Refined lattice parameters of the NPD data of defective UiO-67 at different ND_3 loadings. The maximum standard deviation value of the refined lattice parameters is ± 7.0 x 10^{-4}.

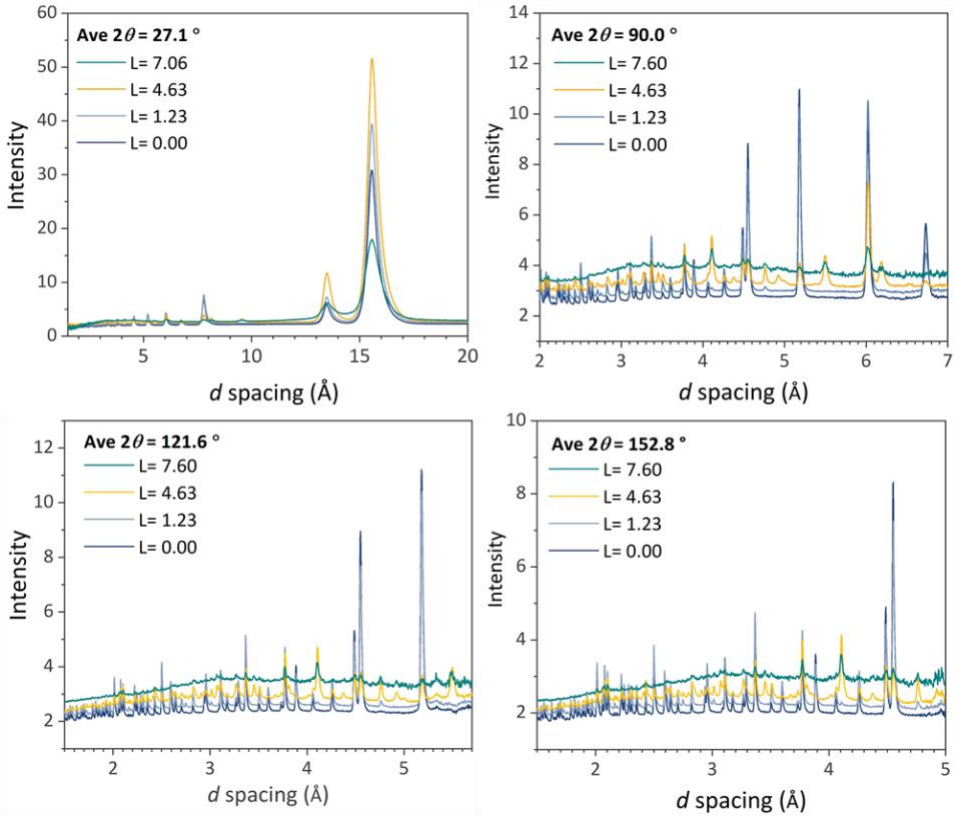

Figure S16 | ND patterns of UiO-67 upon ND_3 adsorption collected at 300 K on the detector banks with different average 2θ values.

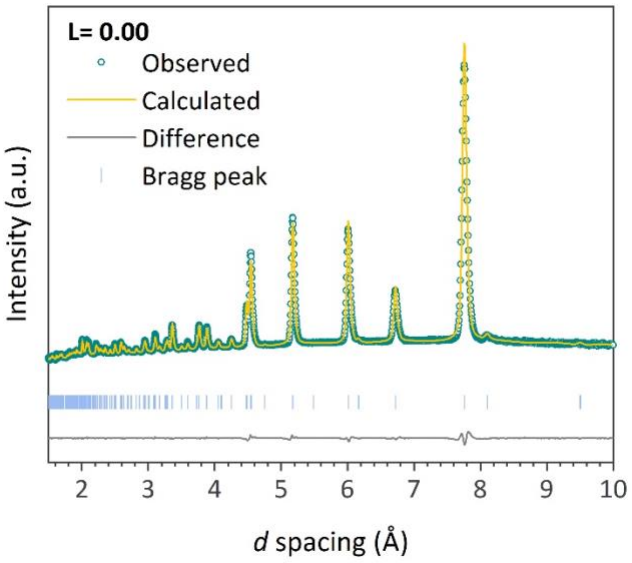

Figure S17 | Fitted ND data of ND_3-free UiO-67 refined by using the data collected at 300 K from the average 2θ = 58.3 ° detector bank.

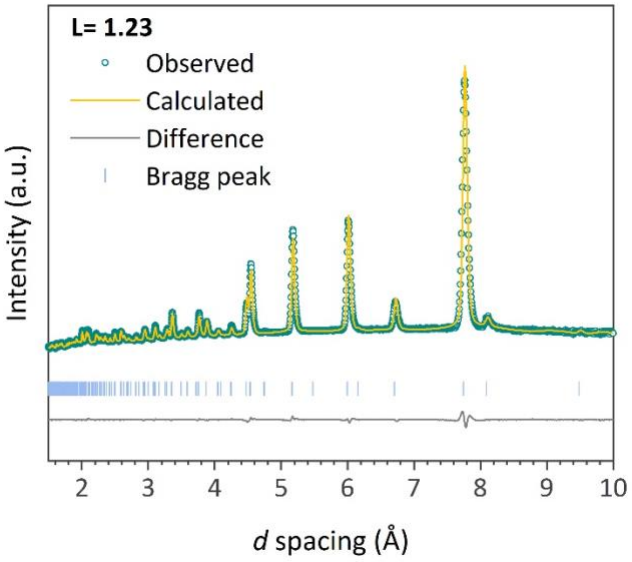

Figure S18 | Fitted ND data of ND_3@UiO-67 at 1.23 mmol/g loading, refined by using the data collected at 300 K from the average 2θ = 58.3 ° detector bank.

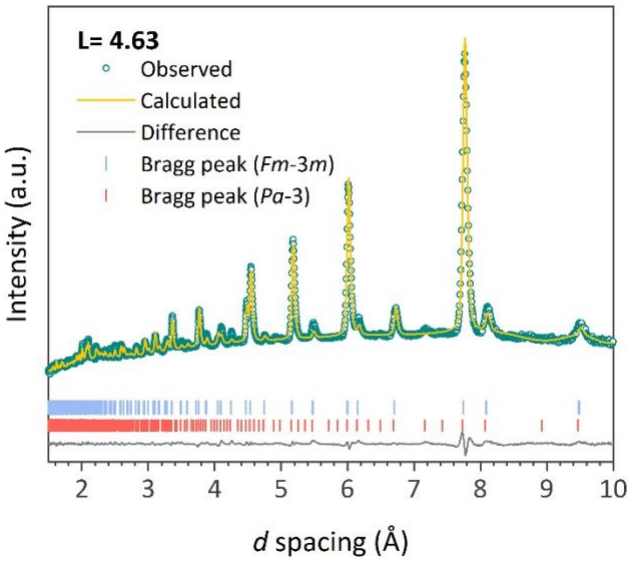

Figure S19 | Fitted ND data of ND_3@UiO-67 at 4.63 mmol/g loading, refined by using the data collected at 300 K from the average $2\theta = 58.3^{\circ}$ detector bank.

At this high ND_3 loading, small but unindexed extra peaks was clearly found in the NPD pattern which is due to the distortion of the cubic Fm-3m MOF structure by the inhomogeneous ND_3 uptake (only a small quantity). Thus, in addition to using the single perfect MOF model (i.e. the model based on published crystal data and the occupancy number of linker with the assumption that the missing linker occurs randomly, the second MOF model with lowering the symmetry to cubic primitive cell (*Pa*-3 space group) to represent a small-distorted phase was applied to achieve the best fit of the structure refinement. The weight percentage of each phase was freely refined to give the final phase composition of 78.16% (*Fm*-3*m*) and 21.84% (*Pa*-3) with all the diffraction peaks well fitted.

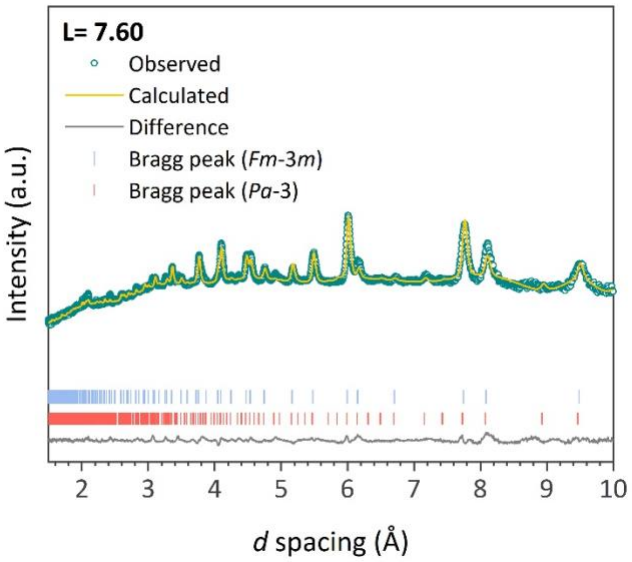

Figure S20 | Fitted ND data of ND_3@UiO-67 at 7.60 mmol/g loading, refined by using the data collected at 300 K from the average $2\theta = 58.3^{o}$ detector bank.

At this high ND_3 loading, small but unindexed extra peaks was clearly found in the NPD pattern which is due to the distortion of the cubic Fm-*3*m MOF structure by the inhomogeneous ND_3 uptake (only a small quantity). Thus, in addition to using the single perfect MOF model (i.e. the model based on published crystal data and the occupancy number of linker with the assumption that the missing linker occurs randomly, the second MOF model with lowering the symmetry to cubic primitive cell (*Pa*-3 space group) to represent a small-distorted phase was applied to achieve the best fit of the structure refinement. The weight percentage of each phase was freely refined to give the final phase composition of 78.16% (*Fm*-3*m*) and 21.84% (*Pa*-3) with all the diffraction peaks well fitted.

Table S1 | Crystallographic data and details of ND_3@UiO-67 samples at various ND_3 dosing.

	Loading amount of ND_3 (mmol/g)			
	0.00	**1.23**	**4.63**	**7.60**
Reticular formula[a]	$Zr_6O_4(OH)_4(bpdc)_4(acetate)_4$			
Crystal system	Cubic			
Space group	*Fm*-3*m*			
Molar mass of MOFs (g/unit cell)[a]	7505.56			
ND_3 per unit cell (molecule)[a]	0.00	9.65	36.3	59.6
Detector	pixellated ^{3}He tube			
Measurement temperature (K)/ Counting time (minutes)	300/20	300/20	300/20	300/20
Refinement method	Rietveld			
Average 2θ for the refinement (°)	58.3			
a=b=c (Å)	26.88(4)	26.83(5)	26.83(7)	26.82(16)
V(Å^3)	19426(8)	19310(10)	19317(15)	19299(3)
R_{wp}/ R_p/ R_{exp} (%)	1.77/1.32/0.47	2.18/1.84/0.38	1.87/1.46/0.50	1.39/1.09/0.49
GOF (χ^2)	3.79	5.68	3.63	2.85

[a] Based on the UiO-67 structure with missing linkers obtained from elemental analyses and ICP-MS results.

Table S2 | *R*-factors and *GOF* values of UiO-67 as a function of ND_3 loading obtained from Rietveld refinement of the associated NPD data recorded at 300 K. UiO-67·*n*ND_3 represents the UiO-67 structure with addition of *n* ND_3 molecule(s) per asymmetric unit. The underlined structures provide the best fit of the refinement

Entry	R_{wp} **(%)**	R_p **(%)**	R_{exp} **(%)**	***GOF***
L= 0.00 at 300 K				
<u>UiO-67</u>	1.77	1.32	0.47	3.79
L= 1.23 at 300 K				
UiO-67	3.14	2.45	0.38	8.26
UiO-67·1ND_3	2.49	1.98	0.38	6.55
<u>UiO-67·2ND_3</u>	2.18	1.84	0.38	5.68
UiO-67·3ND_3	2.47	1.95	0.38	6.50

L= 4.63 at 300 K				
Mixed phases between *Fm*-3*m* (78.16%) and *Pa*-3 (21.84%)				
UiO-67	5.59	3.56	0.50	11.18
UiO-67·1ND_3	4.42	2.65	0.50	8.84
UiO-67·2ND_3	4.10	2.47	0.50	8.20
UiO-67·3ND_3	3.94	2.34	0.50	7.88
UiO-67·4ND_3	3.43	2.12	0.50	6.86
UiO-67·5ND_3 (*Fm*-3*m*) and UiO-67·1ND_3 (*Pa*-3)	1.81	1.46	0.50	3.63
UiO-67·6ND_3	2.24	1.60	0.50	4.08
L= 7.60 at 300 K				
Mixed phases between *Fm*-3*m* (78.16%) and *Pa*-3 (21.84%)				
UiO-67	2.91	1.96	0.49	5.96
UiO-67·1ND_3	2.46	1.59	0.49	5.04
UiO-67·2ND_3	2.14	1.59	0.49	4.39
UiO-67·3ND_3	1.96	1.50	0.49	4.00
UiO-67·4ND_3	1.91	1.51	0.49	3.91
UiO-67·5ND_3 (*Fm*-3*m*) and UiO-67·1ND_3 (*Pa*-3)	1.39	1.09	0.49	2.85
UiO-67·6ND_3	1.50	1.11	0.49	3.06

Table S3 | Summary of Rietveld refinement results of ND_3@UiO-67.

	Loading amount of ND_3 (mmol/g)			
	0.00	**1.23**	**4.63**	**7.60**
Site occupancy factor (per asymmetric unit) of ND_3 at				
Site I	-	0.02	0.04	0.11
Site II	-	0.01	0.01	0.08
Site III	-	-	0.01	0.08
Site IV	-	-	0.02	0.03
Site V	-	-	0.02	0.02
Site I-d[a]	-	-	0.01	0.01

Dihedral angle between two aromatic rings (°)	30.60(1)	32.42(1)	55.20(1)	62.63(2)

[a] This site is created by using a distorted phase (i.e. a lower symmetry phase with a *Pa*-3 space group) which indicates the adsorption of ND_3 at the non-uniform binding sites of UiO-67 caused by missing linker defects.

Table S4 | Structural data from the Rietveld refinement of UiO-67 sample loaded with 1.23 mmol/g ND_3 (9.65 ND_3 molecules per asymmetric unit).

Species	Atom	x	y	z	SOF[a]	B_{eq}[b] (Å^2)	Wyckoff
UiO-67	C4	0.3775(1)	0.0000(1)	0.1168(1)	0.5395(1)	5.3657(7)	96j
	C5	0.3382(1)	0.0000(1)	0.1561(1)	0.5395(1)	5.3657(7)	96j
	C10	0.2902(1)	-0.0121(1)	0.1448(1)	0.4826(1)	4.1290(4)	192l
	H10	0.2818(1)	-0.0206(1)	0.1115(1)	0.4826(1)	4.9548(5)	192l
	C9	0.2541(1)	-0.0122(1)	0.1804(1)	0.4826(1)	4.1290(4)	192l
	H9	0.2206(1)	-0.0207(1)	0.1724(1)	0.4826(1)	4.9548(5)	192l
	C8	0.2672(1)	0.0000(1)	0.2271(1)	0.4826(1)	4.1290(4)	96j
	Zr1	0.5000	0.0000	0.0932	1	3.5338(7)	24e
	O2A	0.4465	-0.0535	0.0535	0.5	0.0100(7)	32f
	O2B	0.4594	-0.0406	0.0406	0.5	0.0100(7)	32f
	H1	0.4284	-0.0716	0.0716	0.5	0.0120(8)	32f
	O1	0.4269	0.0000	0.1336	1	5.4939(6)	96j
Ammonia I	N1rg	-0.1114(2)	0.3889(2)	0.1112(2)	0.0153(2)	5.0000(2)	192l
	H1rg	-0.1312(2)	0.4023(2)	0.0816(2)	0.0153(2)	6.0000(3)	192l
	H2rg	-0.1256(2)	0.4057(2)	0.1423(2)	0.0153(2)	6.0000(3)	192l
	H3rg	-0.1230(2)	0.3530(2)	0.1168(2)	0.0153(2)	6.0000(3)	192l
Ammonia II	N2rg	0.3503(1)	-0.0218(1)	0.3766(1)	0.0098(1)	5.0000(2)	192l
	H4rg	0.3572(1)	-0.0328(1)	0.3408(1)	0.0098(1)	6.0000(3)	192l
	H5rg	0.3130(1)	-0.0144(1)	0.3787(1)	0.0098(1)	6.0000(3)	192l
	H6rg	0.3532(1)	-0.0530(1)	0.3983(1)	0.0098(1)	6.0000(3)	192l

[a] B_{eq} refers to the isotropic displacement factor or the thermal parameter.

[b] SOF represents the site occupancy factor per asymmetric unit.

Table S5 | Structural data from the Rietveld refinement of UiO-67 sample loaded with 4.63 mmol/g ND_3 (36.3 ND_3 molecules per asymmetric unit). Only the structural data obtained from using the cubic *Fm*-3*m* MOF model (major phase) are presented here.

Species	Atom	x	y	z	SOF[a]	B_{eq}[b] (Å^2)	Wyckoff
UiO-67	C4	0.3774(1)	0.0000(1)	0.1168(1)	0.5395(1)	15.000(13)	96j
	C5	0.3381(1)	0.0000(1)	0.1560(1)	0.5395(1)	15.000(13)	96j
	C10	0.2936(1)	-0.0228(1)	0.1482(1)	0.4826(1)	4.2455(7)	192l
	H10	0.2875(1)	-0.0390(1)	0.1172(1)	0.4826(1)	5.0946(9)	192l
	C9	0.2574(1)	-0.0231(1)	0.1837(1)	0.4826(1)	4.2455(7)	192l
	H9	0.2264(1)	-0.0391(1)	0.1781(1)	0.4826(1)	5.0946(9)	192l
	C8	0.2671(1)	0.0000(1)	0.2270(1)	0.4826(1)	4.2455(7)	96j
	Zr1	0.5000	0.0000	0.0932	1	7.8860(13)	24e
	O2A	0.4465	-0.0535	0.0535	0.5	12.151(18)	32f
	O2B	0.4594	-0.0406	0.0406	0.5	12.15118)	32f
	H1	0.4284	-0.0716	0.0716	0.5	14.581(2)	32f
	O1	0.4269	0.0000	0.1336	1	1.3847(7)	96j
Ammonia I	N1rg	-0.1134(2)	0.3864(2)	0.1142(2)	0.0361(2)	3.6561(13)	192l
	H1rg	-0.1377(2)	0.3985(2)	0.0874(2)	0.0361(2)	4.3873(15)	192l
	H2rg	-0.1257(2)	0.4008(2)	0.1473(2)	0.0361(2)	4.3873(15)	192l
	H3rg	-0.1206(2)	0.3494(2)	0.1197(2)	0.0361(2)	4.3873(15)	192l
Ammonia II	N2rg	0.3638(1)	-0.0279(1)	0.3871(1)	0.0071(1)	3.6561(13)	192l
	H4rg	0.3646(1)	-0.0546(1)	0.3510(1)	0.0071(1)	4.3873(15)	192l
	H5rg	0.3278(1)	-0.0258(1)	0.3994(1)	0.0071(1)	4.3873(15)	192l
	H6rg	0.3814(1)	-0.0428(1)	0.4175(1)	0.0071(1)	4.3873(15)	192l
Ammonia III	N3rg	0.9445(2)	1.0300(2)	1.0549(2)	0.0238(2)	3.6561(13)	192l
	H7rg	0.9203(2)	1.0049(2)	1.0702(2)	0.0238(2)	4.3873(15)	192l
	H8rg	0.9659(2)	1.0434(2)	1.0835(2)	0.0238(2)	4.3873(15)	192l
	H9rg	0.9705(2)	1.0099(2)	1.0357(2)	0.0238(2)	4.3873(15)	192l
Ammonia IV	N4rg	0.1935(2)	0.1984(2)	0.2050(2)	0.0122(2)	3.6561(13)	192l
	H10rg	0.2204(2)	0.2191(2)	0.2223(2)	0.0122(2)	4.3873(15)	192l
	H11rg	0.1767(2)	0.2214(2)	0.1797(2)	0.0122(2)	4.3873(15)	192l
	H12rg	0.2116(2)	0.1745(2)	0.1815(2)	0.0122(2)	4.3873(15)	192l
Ammonia V	N5rg	2.8167(1)	-0.5892(1)	2.5731(1)	0.0186(1)	3.6561(13)	192l
	H13rg	2.7941(1)	-0.5962(1)	2.5433(1)	0.0186(1)	4.3873(15)	192l

	H14rg	2.8334(1)	-0.5556(1)	2.5666(1)	0.0186(1)	4.3873(15)	192l
	H15rg	2.7939(1)	-0.5801(1)	2.6022(1)	0.0186(1)	4.3873(15)	192l

[a] B_{eq} refers to the isotropic displacement factor or the thermal parameter.

[b] SOF represents the site occupancy factor per asymmetric unit.

Table S6 | Structural data from the Rietveld refinement of UiO-67 sample loaded with 7.60 mmol/g ND_3 (59.6 ND_3 molecules per asymmetric unit). Only the structural data obtained from using the cubic *Fm*-3*m* MOF model (major phase) are presented here.

Species	Atom	x	y	z	SOF[a]	B_{eq}[b] (Å^2)	Wyckoff
UiO-67	C4	0.3775(2)	0.0000(2)	0.1168(2)	0.5416(2)	8.0000(17)	96j
	C5	0.3382(2)	0.0000(2)	0.1561(2)	0.5416(2)	8.0000(17)	96j
	C10	0.2926(2)	-0.0202(2)	0.1472(2)	0.4838(2)	7.3467(1)	192l
	H10	0.2858(2)	-0.0344(2)	0.1154(2)	0.4838(2)	8.8160(1)	192l
	C9	0.2564(2)	-0.0204(2)	0.1827(2)	0.4838(2)	7.3467(1)	192l
	H9	0.2246(2)	-0.0345(2)	0.1764(2)	0.4838(2)	8.8160(1)	192l
	C8	0.2672(2)	0.0000(2)	0.2271(2)	0.4838(2)	7.3467(1)	96j
	Zr1	0.5000	0.0000	0.0932	1	0.0100(3)	24e
	O2A	0.4465	-0.0535	0.0535	0.5	0.0100(3)	32f
	O2B	0.4594	-0.0406	0.0406	0.5	0.0100(3)	32f
	H1	0.4284	-0.0716	0.0716	0.5	0.0120(4)	32f
	O1	0.4269	0.0000	0.1336	1	8.0000(2)	96j
Ammonia I	N1rg	-0.1288(2)	0.3875(2)	0.1093(2)	0.1086(2)	5.0000(14)	192l
	H1rg	-0.1526(2)	0.4006(2)	0.0826(2)	0.1086(2)	6.0000(17)	192l
	H2rg	-0.1414(2)	0.4008(2)	0.1426(2)	0.1086(2)	6.0000(17)	192l
	H3rg	-0.1363(2)	0.3504(2)	0.1134(2)	0.1086(2)	6.0000(17)	192l
Ammonia II	N2rg	0.3436(2)	-0.0281(2)	0.3905(2)	0.0811(1)	5.0000(14)	192l

	H4rg	0.3386(2)	-0.0544(2)	0.3633(2)	0.0811(1)	6.0000(17)	192l
	H5rg	0.3089(2)	-0.0158(2)	0.4002(2)	0.0811(1)	6.0000(17)	192l
	H6rg	0.3543(2)	-0.0468(2)	0.4219(2)	0.0811(1)	6.0000(17)	192l
Ammonia III	N3rg	0.9046(1)	1.0418(1)	0.7737(1)	0.0775(1)	5.0000(14)	192l
	H7rg	0.8917(1)	1.0413(1)	0.8096(1)	0.0775(1)	6.0000(17)	192l
	H8rg	0.9346(1)	1.0184(1)	0.7726(1)	0.0775(1)	6.0000(17)	192l
	H9rg	0.8796(1)	1.0220(1)	0.7528(1)	0.0775(1)	6.0000(17)	192l
Ammonia IV	N4rg	0.1879(1)	0.2043(1)	0.2143(1)	0.0334(1)	5.0000(14)	192l
	H10rg	0.1807(1)	0.1784(1)	0.2413(1)	0.0334(1)	6.0000(17)	192l
	H11rg	0.2226(1)	0.2182(1)	0.2214(1)	0.0334(1)	6.0000(17)	192l
	H12rg	0.1947(1)	0.1850(1)	0.1821(1)	0.0334(1)	6.0000(17)	192l
Ammonia V	N5rg	0.9686(1)	0.9833(1)	1.0445(1)	0.0200(1)	5.0000(14)	192l
	H13rg	0.9424(1)	1.0089(1)	1.0550(1)	0.0200(1)	6.0000(17)	192l
	H14rg	0.9498(1)	0.9511(1)	1.0363(1)	0.0200(1)	6.0000(17)	192l
	H15rg	0.9804(1)	0.9934(1)	1.0097(1)	0.0200(1)	6.0000(17)	192l

[a] B_{eq} refers to the isotropic displacement factor or the thermal parameter.

[b] SOF represents the site occupancy factor per asymmetric unit.

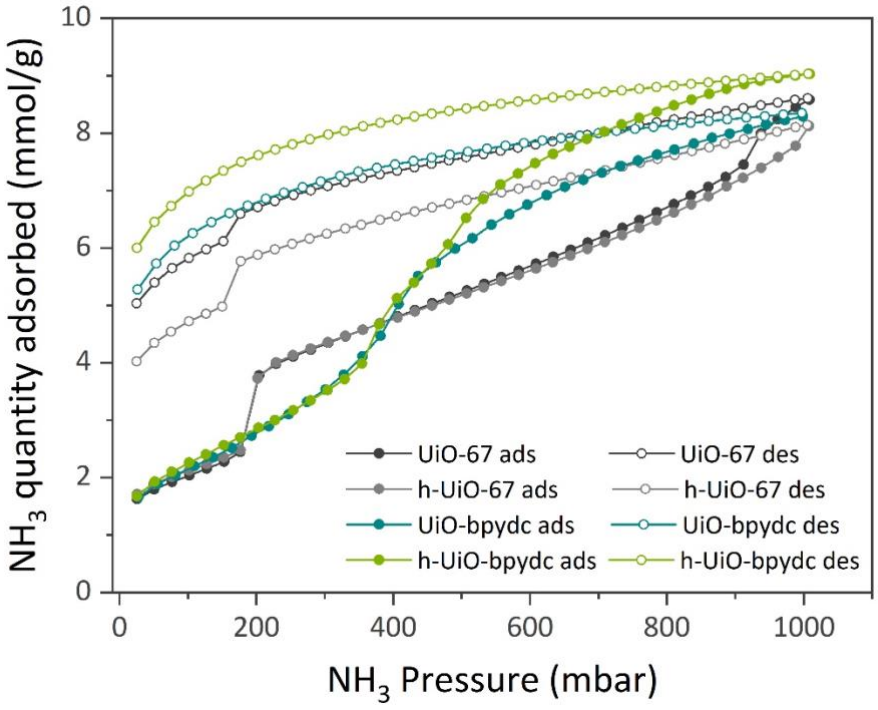

Figure S21 | Uptake data for NH_3 adsorption of MOF samples before and after the healing process with different batches of samples from that of Fig. 2 and Fig. 3 in the main manuscript. The isotherms were measured from 0 to 1000 mbar of NH_3 pressure at 298 K showing the similar sorption profiles as shown in the main manuscript. The healed samples are denoted with h alphabet. Adsorption and desorption branches are labeled as ads and des, respectively. For UiO-67 sample, the two stepped uptakes at ~200 mbar and at ~800 mbar can also be seen, however, due to the different nature and smaller quantity of defects in this sample (~1 missing linker out of 6 by ICP-MS) smaller step changes occur at slightly different pressures. Notice that the second transition was disappeared from the healed UiO67, which was due to the total repair of the missing linker during healing (ICP-MS). On the other hand, the NH_3 uptake of the healed UiO-bpydc increased from 8.4 to 9.0 $mmolg^{-1}$ with no significant change of the transition pressure. This result could be explained by the increase of NH_3 binding sites due to more bipyridine linkers available for binding in the healed UiO-bpydc.

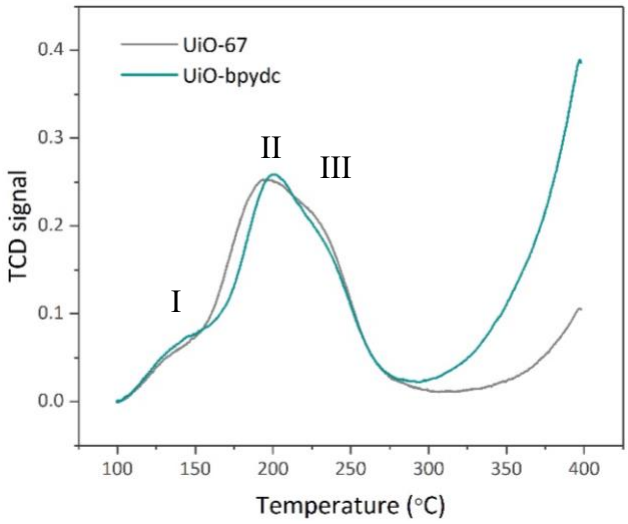

Figure S22 | Normalised NH_3-TPD curves of defective MOF samples, measured with a heating rate of 10 °C/min.

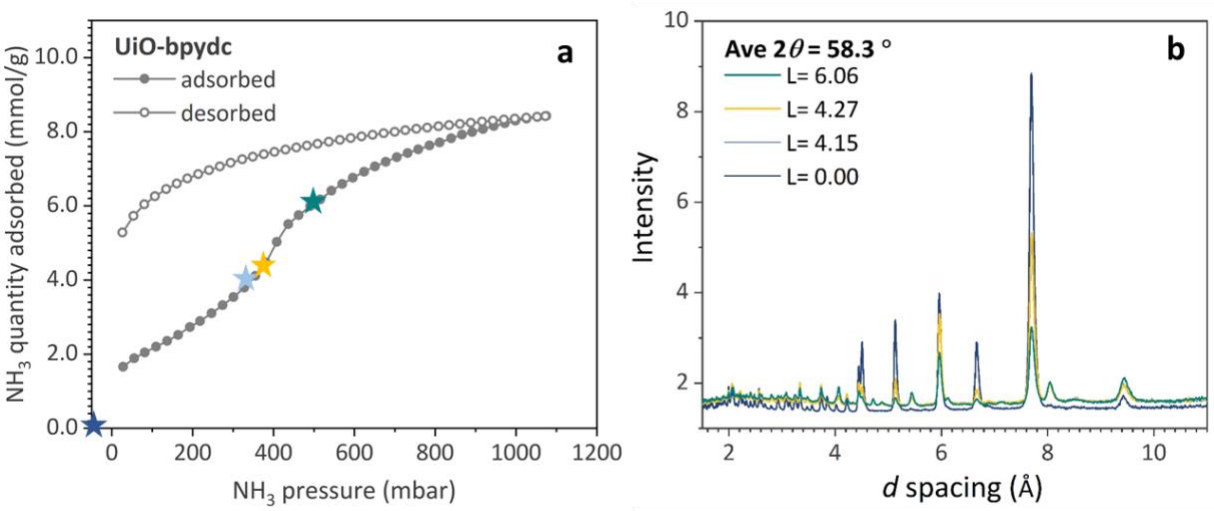

Figure S23 | *In situ* NPD patterns of defective UiO-bpydc at various loadings of ND_3: (a) Each dosing point was marked as a star symbol in the stepwise NH_3 adsorption isotherm measured at 298 K and up to 1100 mbar of NH_3 pressure; (b) corresponding NPD patterns collected at 300 K on the average $2\theta = 58.3^{\circ}$ detector bank. L refers to the dosing amount of ND_3 in mmol/g.

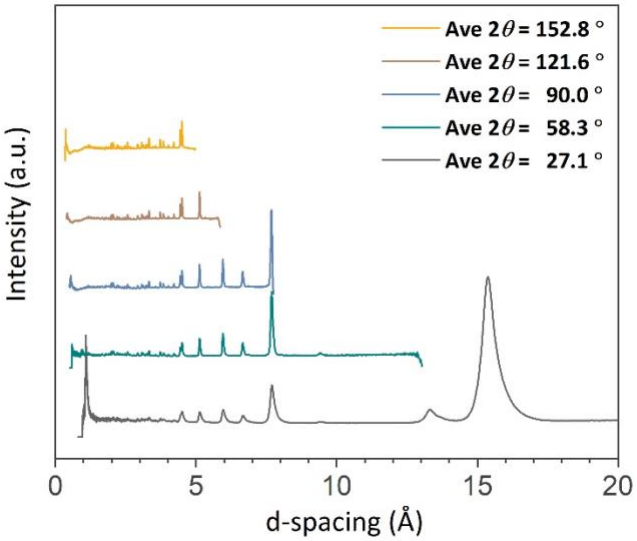

Figure S24 | ND patterns of ND_3-free UiO-bpydc recorded at 300 K by using different detector banks. Ave 2θ refers to the average 2θ of the detector banks.

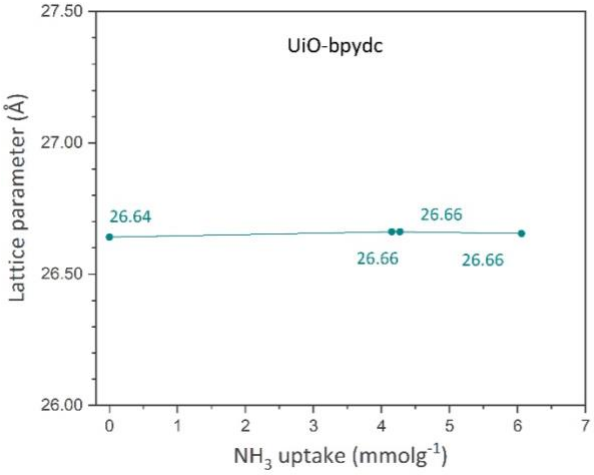

Figure S25 | Refined lattice parameters of the NPD data of defective UiO-bpydc at different ND_3 loadings. The maximum standard deviation value of the refined lattice parameters is ± 7.0 x 10^{-4}.

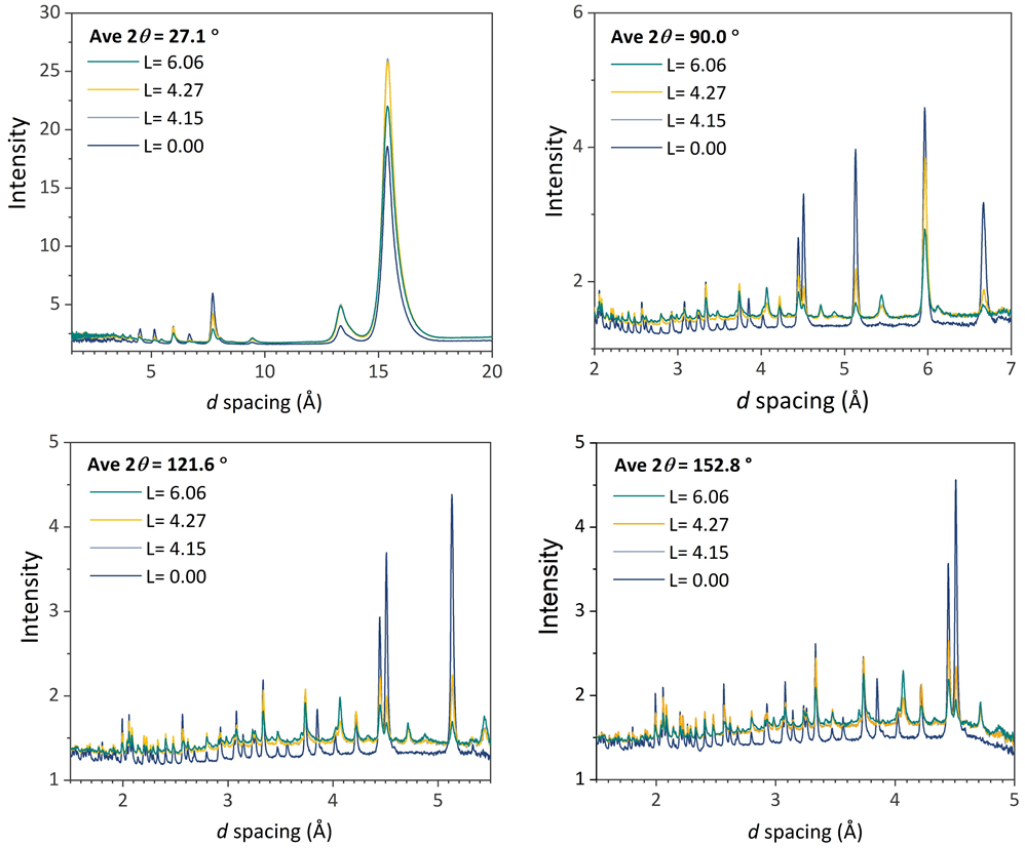

Figure S26 | ND patterns of UiO-bpydc upon ND_3 adsorption collected at 300 K on the detector banks with different average 2θ values.

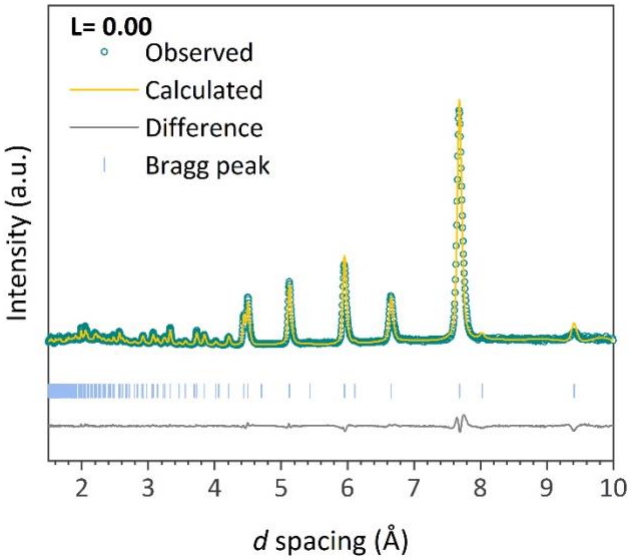

Figure S27 | Fitted ND data of ND_3-free UiO-bpydc, refined by using the data collected at 300 K from the average 2θ = 58.3 º detector bank.

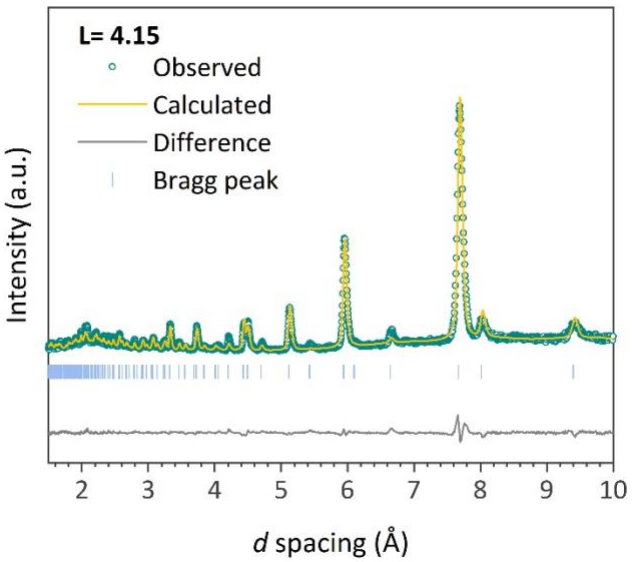

Figure S28 | Fitted ND data of ND_3@UiO-bpydc at 4.15 mmol/g loading, refined by using the data collected at 300 K from the average 2θ = 58.3 º detector bank.

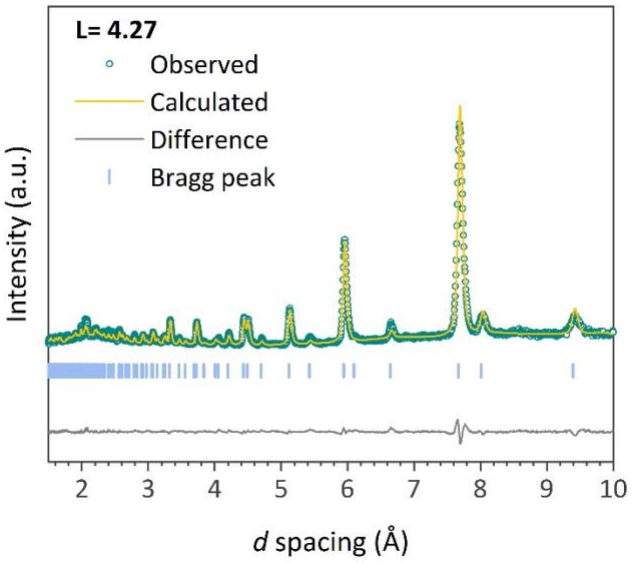

Figure S29 | Fitted ND data of ND_3@UiO-bpydc at 4.27 mmol/g loading, refined by using the data collected at 300 K from the average 2θ = 58.3 º detector bank.

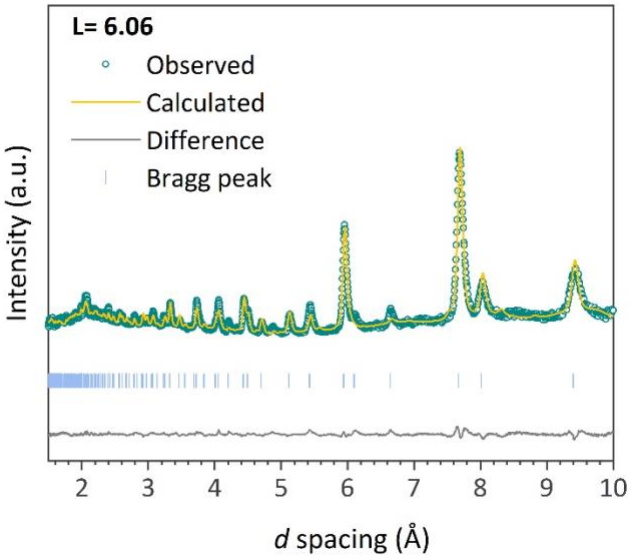

Figure S30 | Fitted ND data of ND_3@UiO-bpydc at 6.06 mmol/g loading, refined by using the data collected at 300 K from the average 2θ = 58.3 º detector bank.

Table S7 | Crystallographic data and details of ND_3@UiO-bpydc samples at various ND_3 dosing.

	Loading amount of ND_3 (mmol/g)			
	0.00	**4.15**	**4.27**	**6.06**
Reticular formula[a]	$Zr_6O_4(OH)_4(bpydc)_{4.5}(acetate)_3$			
Crystal system	Cubic			
Space group	*Fm*-3*m*			
Molar mass of MOFs (g/unit cell)[a]	7785.36			
ND_3 per unit cell (molecule)[a]	0.00	32.6	33.6	47.6
Detector	pixellated ^{3}He tube			
Measurement temperature (K)/ Counting time (minutes)	300/20			
Refinement method	Rietveld			
Average 2θ for the refinement (°)	58.3			
a=b=c (Å)	26.62(7)	26.57(7)	26.58(7)	26.57 (12)
V(Å^3)	18869(14)	18768(16)	18771(15)	18764(3)
R_{wp}/ R_p/ R_{exp} (%)	2.56/1.82/0.77	1.99/1.66/0.75	1.66/1.41/0.61	1.55/1.30/0.53
GOF (χ^2)	2.80	2.66	2.74	2.94

[a] Based on the UiO-bpydc structure with missing linkers obtained from elemental analyses and ICP-MS results.

Table S8 | *R*-factors and *GOF* values of UiO-bpydc as a function of ND_3 loading obtained from Rietveld refinement of the associated NPD data recorded at 300 K. UiO-bpydc·*n*ND_3 represents the UiO-bpydc structure with addition of *n* ND_3 molecule(s) per asymmetric unit. The underlined structures provide the best fit of the refinement.

Entry	R_{wp} **(%)**	R_p **(%)**	R_{exp} **(%)**	***GOF***
L= 0.00 at 300 K				
UiO-bpydc	2.56	1.82	0.77	2.80
L= 4.15 at 300K				
UiO-bpydc	6.90	2.55	0.75	9.20
UiO-bpydc·1ND_3	6.13	2.46	0.75	8.17
UiO-bpydc·2ND_3	4.78	1.93	0.75	5.97

UiO-bpydc·3ND_3	1.99	1.66	0.75	2.66
UiO-bpydc·4ND_3	3.68	1.66	0.75	4.90
L= 4.27 at 300 K				
UiO-bpydc	5.72	2.59	0.61	9.38
UiO-bpydc·1ND_3	5.45	2.36	0.61	8.93
UiO-bpydc·2ND_3	5.42	2.45	0.61	8.88
UiO-bpydc·3ND_3	5.31	2.85	0.61	8.70
UiO-bpydc·4ND_3	1.66	1.41	0.61	2.74
UiO-bpydc·5ND_3	4.06	1.97	0.61	6.66
L= 6.06 at 300 K				
UiO-bpydc	3.55	2.42	0.53	6.70
UiO-bpydc·1ND_3	3.49	2.17	0.53	6.58
UiO-bpydc·2ND_3	3.27	2.07	0.53	6.17
UiO-bpydc·3ND_3	2.50	1.95	0.53	4.72
UiO-bpydc·4ND_3	2.15	1.64	0.53	4.06
UiO-bpydc·5ND_3	1.55	1.31	0.53	2.94
UiO-bpydc·6ND_3 *too close to the N3 site*	2.02	1.59	0.53	3.81

Table S9 | Summary of the Rietveld refinement results of ND_3@UiO-bpydc samples.

	Loading amount of ND_3 (mmol/g)			
	0.00	**4.15**	**4.27**	**6.06**
Site occupancy factor per asymmetric unit of ND_3 at				
Site I’	-	0.08	0.07	0.10
Site II’	-	0.02	0.03	0.08
Site III’	-	0.01	0.01	0.01
Site IV’	-	-	0.01	0.03
Site V’	-	-	-	0.04
Dihedral angle between two aromatic rings (°)	21.80(1) 20.33 (DFT)	19.95(1)	16.77(3)	10.00(4)

Table S10 | Structural data from the Rietveld refinement of UiO-bpydc sample loaded with 4.15 mmol/g ND_3 (32.6 ND_3 molecules per asymmetric unit).

Species	Atom	x	y	z	SOF[a]	B_{eq}[b] (Å^2)	Wyckoff
UiO-bpydc	C4	0.3811(2)	0.0000(2)	0.1179(2)	0.6667(2)	8.0000(12)	96j
	C5	0.3411(2)	0.0000(2)	0.1576(2)	0.6667(2)	8.0000(12)	96j
	C10	0.2919(2)	-0.0042(2)	0.1451(2)	0.4855(2)	0.0100(6)	192l
	H10	0.2826(2)	-0.0071(2)	0.1107(2)	0.4855(2)	0.0120(8)	192l
	N9	0.2554(2)	-0.0042(2)	0.1810(2)	0.2428(2)	0.0100(6)	192l
	C9	0.2554(2)	-0.0042(2)	0.1810(2)	0.2428(2)	0.0100(6)	192l
	H9	0.2209(2)	-0.0071(2)	0.1722(2)	0.2428(2)	0.0120(8)	192l
	C8	0.2697(2)	0.0000(2)	0.2292(2)	0.4855(2)	0.0100(6)	96j
	Zr1	0.5000	0.0000	0.0932	1	0.0100(11)	24e
	O2A	0.4465	-0.0535	0.0535	0.5	0.0100(13)	32f
	O2B	0.4594	-0.0406	0.0406	0.5	0.0100(143	32f
	H1	0.4284	-0.0716	0.0716	0.5	0.0100(16)	32f
	O1	0.4269	0.0000	0.1336	1	0.0100(10)	96j
Ammonia I’	N1rg	0.1180(1)	0.3831(1)	0.1168(1)	0.0751(1)	0.0100(9)	192l
	H1rg	0.1550(1)	0.3831(1)	0.1063(1)	0.0751(1)	0.0120(11)	192l
	H2rg	0.1070(1)	0.3462(1)	0.1183(1)	0.0751(1)	0.0120(11)	192l
	H3rg	0.1170(1)	0.3921(1)	0.1542(1)	0.0751(1)	0.0120(11)	192l
Ammonia II’	N2rg	0.3723(1)	-0.0457(1)	0.3413(1)	0.0219(1)	0.0100(9)	192l
	H4rg	0.3901(1)	-0.0159(1)	0.3579(1)	0.0219(1)	0.0120(11)	192l
	H5rg	0.3604(1)	-0.0336(1)	0.3068(1)	0.0219(1)	0.0120(11)	192l
	H6rg	0.3996(1)	-0.0709(1)	0.3316(1)	0.0219(1)	0.0120(11)	192l
	N3rg	0.4549(1)	-0.0740(1)	0.3333(2)	0.0098(3)	0.0100(9)	192l

Ammonia III'	H7rg	0.4843(1)	-0.0557(1)	0.3501(2)	0.0098(3)	0.0120(11)	192l
	H8rg	0.4502(1)	-0.0579(1)	0.2987(2)	0.0098(3)	0.0120(11)	192l
	H9rg	0.4680(1)	-0.1088(1)	0.3232(2)	0.0098(3)	0.0120(11)	192l

[a] B_{eq} refers to the isotropic displacement factor or the thermal parameter.

[b] SOF represents the site occupancy factor per asymmetric unit.

Table S11 | Structural data from the Rietveld refinement of UiO-bpydc sample loaded with 4.27 mmol/g ND_3 (33.6 ND_3 molecules per asymmetric unit).

Species	**Atom**	**x**	**y**	**z**	**SOF[a]**	***B*eq[b] (Å^2)**	**Wyckoff**
UiO-bpydc	C4	0.3811(1)	0.0000(1)	0.1179(1)	0.6667(1)	8.0000(11)	96j
	C5	0.3414(1)	0.0000(1)	0.1575(1)	0.6667(1)	8.0000(11)	96j
	C10	0.2921(1)	-0.0066(1)	0.1454(1)	0.4855(1)	0.0100(5)	192l
	H10	0.2830(1)	-0.0113(1)	0.1111(1)	0.4855(1)	0.0120(6)	192l
	N9	0.2556(1)	-0.0067(1)	0.1812(1)	0.2428(1)	0.0100(5)	192l
	C9	0.2556(1)	-0.0067(1)	0.1812(1)	0.2428(1)	0.0100(5)	192l
	H9	0.2212(1)	-0.0114(1)	0.1726(1)	0.2428(1)	0.0120(6)	192l
	C8	0.2697(1)	0.0000(1)	0.2292(1)	0.4855(1)	0.0100(5)	96j
	Zr1	0.5000	0.0000	0.0932	1	0.0100(9)	24e
	O2A	0.4465	-0.0535	0.0535	0.5	0.0100(11)	32f
	O2B	0.4594	-0.0406	0.0406	0.5	0.0100(11)	32f
	H1	0.4284	-0.0716	0.0716	0.5	0.0100(13)	32f
	O1	0.42693	0.0000	0.13363	1	0.0100(8)	96j
Ammonia I'	N1rg	-0.1129(1)	0.3809(1)	0.1199(1)	0.0736(1)	0.0100(1)	192l
	H1rg	-0.1123(1)	0.3418(1)	0.1201(1)	0.0736(1)	0.0120(1)	192l
	H2rg	-0.0801(1)	0.3930(1)	0.1374(1)	0.0736(1)	0.0120(1)	192l

	H3rg	-0.1059(1)	0.3922(1)	0.0831(1)	0.0736(1)	0.0120(1)	192l
Ammonia II'	N2rg	0.3605(2)	0.0010(2)	0.3377(2)	0.0308(3)	0.0100(1)	192l
	H4rg	0.3711(2)	-0.0191(2)	0.3138(2)	0.0308(3)	0.0120(1)	192l
	H5rg	0.3615(2)	0.0426(2)	0.3162(2)	0.0308(3)	0.0120(1)	192l
	H6rg	0.3222(2)	0.0054(2)	0.3439(2)	0.0308(3)	0.0120(1)	192l
Ammonia III'	N3rg	0.4609(2)	0.0754(2)	0.3354(2)	0.0134(1)	0.0100(1)	192l
	H7rg	0.4320(2)	0.0491(2)	0.3353(2)	0.0134(1)	0.0120(1)	192l
	H8rg	0.4611(2)	0.0924(2)	0.3002(2)	0.0134(1)	0.0120(1)	192l
	H9rg	0.4494(2)	0.1050(2)	0.3583(2)	0.0134(1)	0.0120(1)	192l
Ammonia IV'	N4rg	0.4702(2)	0.0655(2)	0.4865(2)	0.0090(1)	0.0100(1)	192l
	H10rg	0.4535(2)	0.0691(2)	0.4513(2)	0.0090(1)	0.0120(1)	192l
	H11rg	0.4910(2)	0.0325(2)	0.4859(2)	0.0090(1)	0.0120(1)	192l
	H12rg	0.4988(2)	0.0920(2)	0.4883(2)	0.0090(1)	0.0120(1)	192l

[a] B_{eq} refers to the isotropic displacement factor or the thermal parameter.

[b] SOF represents the site occupancy factor per asymmetric unit.

Table S12 | Structural data from the Rietveld refinement of UiO-bpydc sample loaded with 6.06 mmol/g ND_3 (47.6 ND_3 molecules per asymmetric unit).

Species	**Atom**	**x**	**y**	**z**	**SOF[a]**	B_{eq}[b] (Å^2)	**Wyckoff**
UiO-bpydc	C4	0.3810(2)	-0.0000(2)	0.1178(2)	0.6667(2)	8.0000(13)	96j
	C5	0.3413(2)	-0.0000(2)	0.1575(2)	0.6667(2)	8.0000(13)	96j
	C10	0.3536(2)	-0.0056(2)	0.2068(2)	0.4855(2)	0.0100(11)	192l
	H10	0.3879(2)	-0.0096(2)	0.2160(2)	0.4855(2)	0.0120(14)	192l

	N9	0.3178(2)	-0.0057(2)	0.2434(2)	0.2428(2)	0.0100(11)	192l
	C9	0.3178(2)	-0.0057(2)	0.2434(2)	0.2428(2)	0.0100(11)	192l
	H9	0.3265(2)	-0.0096(2)	0.2778(2)	0.2428(2)	0.0120(14)	192l
	C8	0.2696(2)	0.0000(2)	0.2292(2)	0.4855(2)	0.0100(11)	96j
	Zr1	0.5000	0.0000	0.0932	1	0.0100(11)	24e
	O2A	0.4465	-0.0535	0.0535	0.5	0.0100(13)	32f
	O2B	0.4594	-0.0406	0.0406	0.5	0.0100(13)	32f
	H1	0.4234	-0.0766	0.0766	0.5	0.0100(16)	32f
	O1	0.4269	0.0000	0.1336	1	0.0100(10)	96j
Ammonia I’	N1rg	-0.1129(2)	0.3809(2)	0.1199(2)	0.0975(1)	0.0100(10)	192l
	H1rg	-0.1032(2)	0.3774(2)	0.1560(2)	0.0975(1)	0.0120(12)	192l
	H2rg	-0.0931(2)	0.3554(2)	0.1006(2)	0.0975(1)	0.0120(12)	192l
	H3rg	-0.1476(2)	0.3666(2)	0.1164(2)	0.0975(1)	0.0120(12)	192l
Ammonia II’	N2rg	0.3605(3)	0.0010(3)	0.3377(3)	0.0771(2)	0.0100(10)	192l
	H4rg	0.3771(3)	0.0268(3)	0.3066(3)	0.0771(2)	0.0120(12)	192l
	H5rg	0.3744(3)	-0.0266(3)	0.3390(3)	0.0771(2)	0.0120(12)	192l
	H6rg	0.3774(3)	0.0262(3)	0.3691(3)	0.0771(2)	0.0120(12)	192l
Ammonia III’	N3rg	0.4488(3)	0.0738(3)	0.3331(3)	0.0134(2)	0.0100(10)	192l
	H7rg	0.4193(3)	0.0508(3)	0.3291(3)	0.0134(2)	0.0120(12)	192l
	H8rg	0.4710(3)	0.0685(3)	0.3032(3)	0.0134(2)	0.0120(12)	192l
	H9rg	0.4364(3)	0.1088(3)	0.3272(3)	0.0134(2)	0.0120(12)	192l
Ammonia IV’	N4rg	0.4728(2)	-0.0138(2)	0.4222(2)	0.0304(4)	0.0100(10)	192l
	H10rg	0.4660(2)	-0.0512(2)	0.4132(2)	0.0304(4)	0.0120(12)	192l

	H11rg	0.4402(2)	0.0065(2)	0.4150(2)	0.0304(4)	0.0120(12)	192l
	H12rg	0.4747(2)	-0.0109(2)	0.4612(2)	0.0304(4)	0.0120(12)	192l
Ammonia V'	N5rg	0.2465(3)	0.2536(3)	0.2561(3)	0.0397(3)	0.0100(10)	192l
	H13rg	0.2409(3)	0.2227(3)	0.2354(3)	0.0397(3)	0.0120(12)	192l
	H14rg	0.2531(3)	0.2818(3)	0.2321(3)	0.0397(3)	0.0120(12)	192l
	H15rg	0.2131(3)	0.2639(3)	0.2698(3)	0.0397(3)	0.0120(12)	192l

[a] B_{eq} refers to the isotropic displacement factor or the thermal parameter.

[b] SOF represents the site occupancy factor per asymmetric unit.

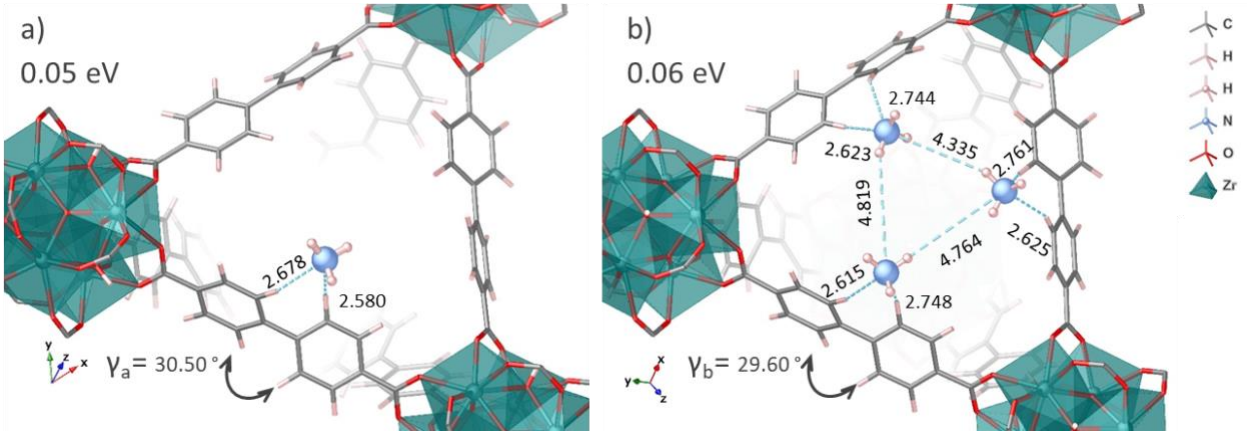

Figure S31 | DFT optimised structures of non-defective UiO-67 with *n* NH_3 molecules at the trigonal window: **a**) *n*= 1 and **b**) *n*= 3. The corresponding binding energies are depicted at the top left of each image. The units of the H bond lengths and the specific atom−atom distances are in angstrom (Å). The dihedral angles between two aromatic rings are denoted as γ.

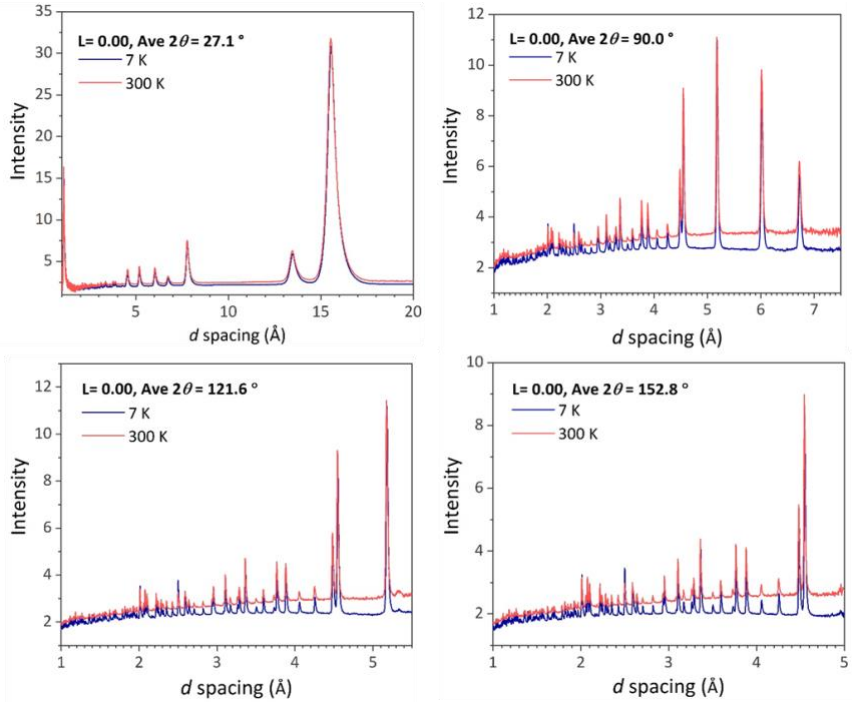

Figure S32 | *In situ* NPD patterns of UiO-67 before ND_3 loading measured at 7 K (blue line) and 300 K (red line). The data were collected from different detector banks.

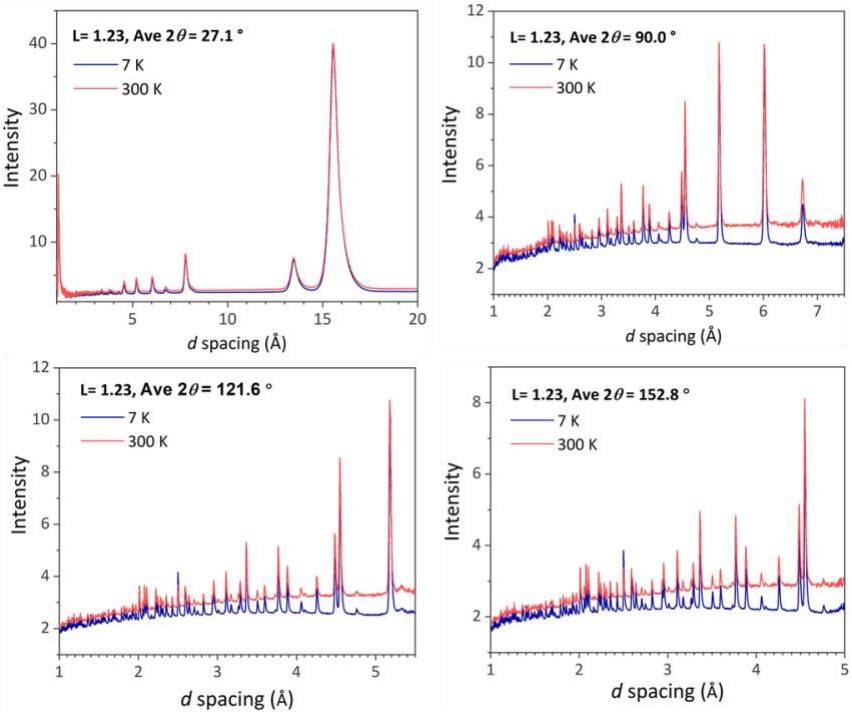

Figure S33 | *In situ* NPD patterns of UiO-67 at ND_3 loading (L) of 1.23 mmol/g measured at 7 K (blue line) and 300 K (red line). The data were collected from different detector banks.

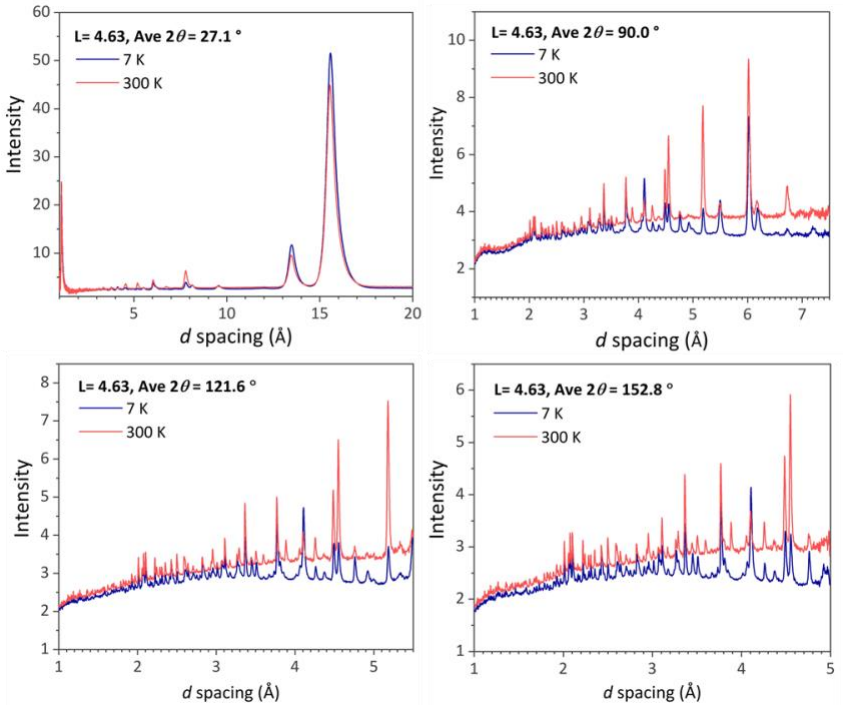

Figure S34 | *In situ* NPD patterns of UiO-67 at ND_3 loading (L) of 4.63 mmol/g measured at 7 K (blue line) and 300 K (red line). The data were collected from different detector banks.

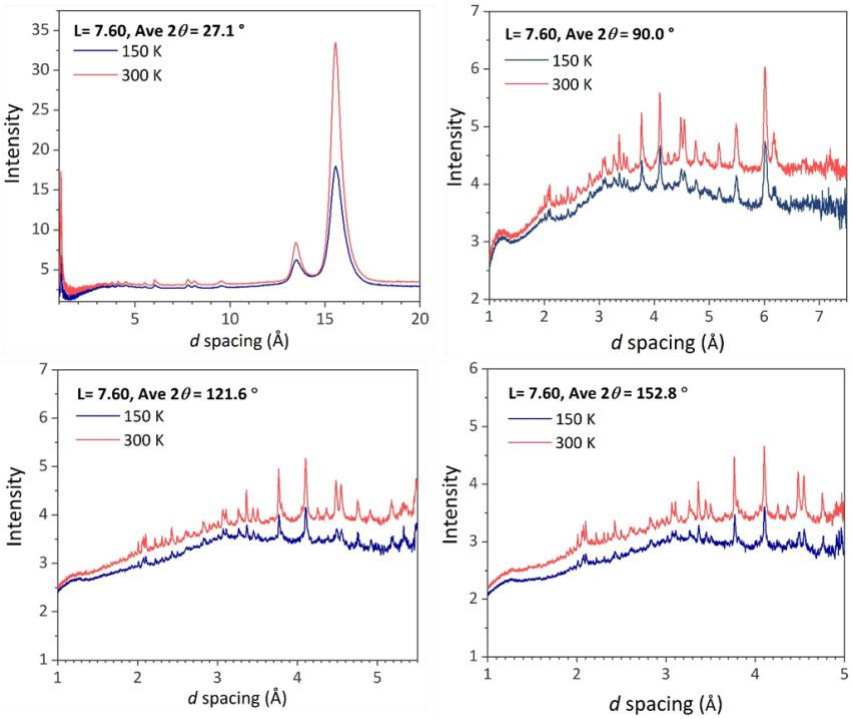

Figure S35 | *In situ* NPD patterns of UiO-67 at ND_3 loading (L) of 7.60 mmol/g measured at 150 K (blue line) and 300 K (red line). The data were collected from different detector banks.

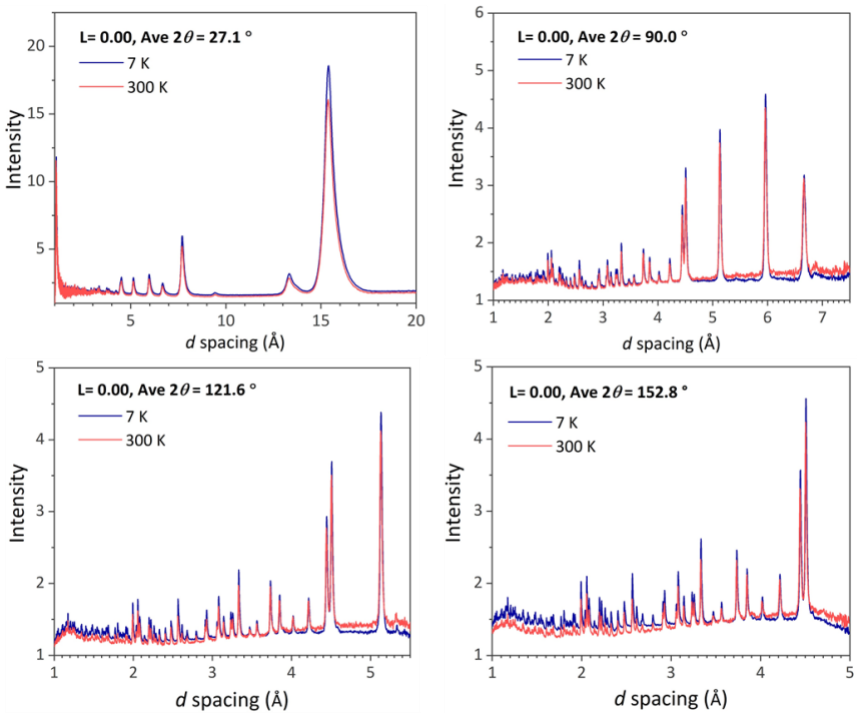

Figure S36 | *In situ* NPD patterns of UiO-bpydc before ND_3 loading measured at 7 K (blue line) and 300 K (red line). The data were collected from different detector banks.

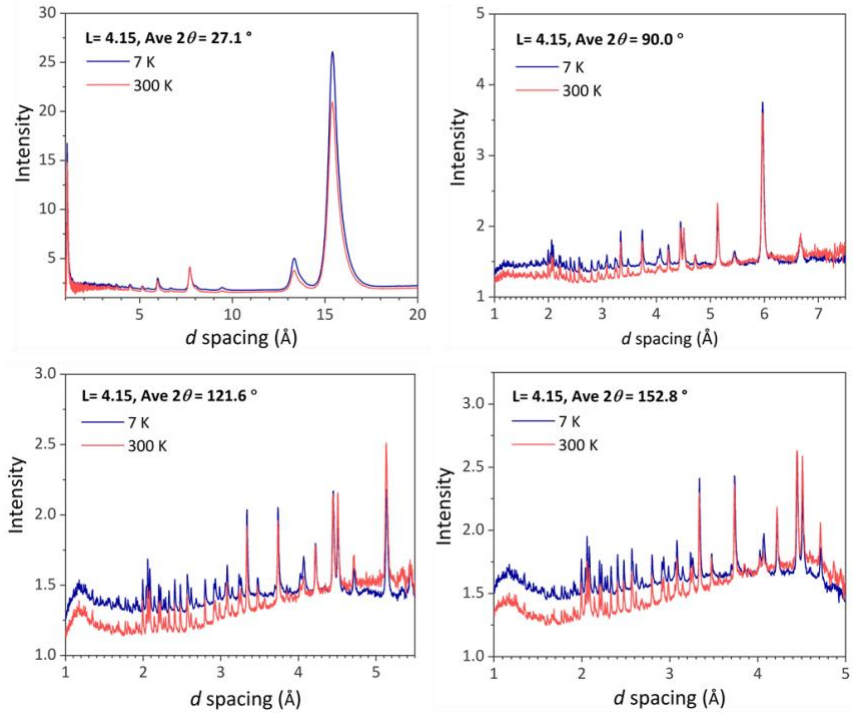

Figure S37 | *In situ* NPD patterns of UiO-bpydc at ND_3 loading (L) of 4.15 mmol/g measured at 7 K (blue line) and 300 K (red line). The data were collected from different detector banks.

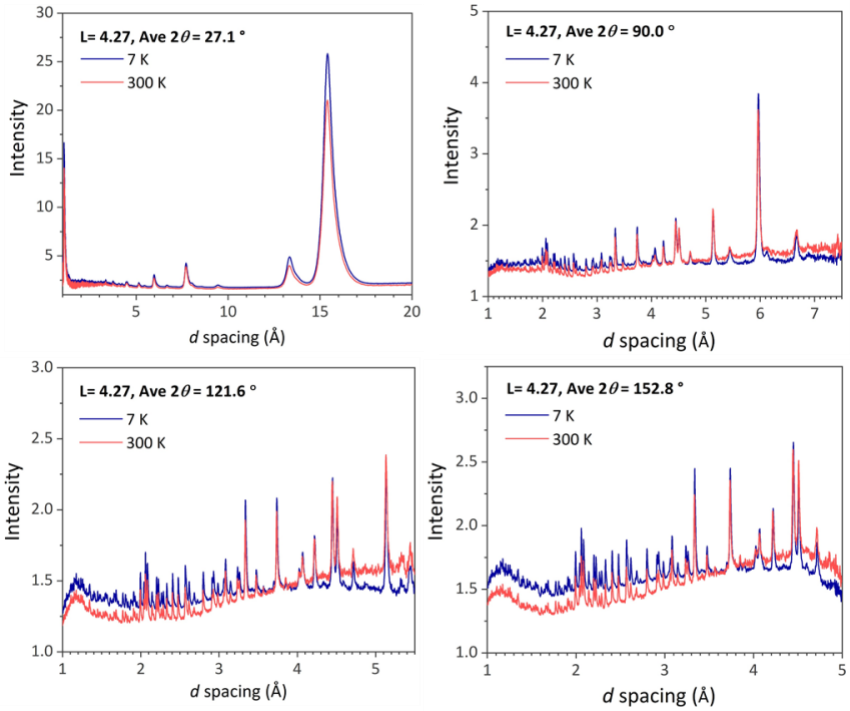

Figure S38 | *In situ* NPD patterns of UiO-bpydc at ND_3 loading (L) of 4.27 mmol/g measured at 7 K (blue line) and 300 K (red line). The data were collected from different detector banks.

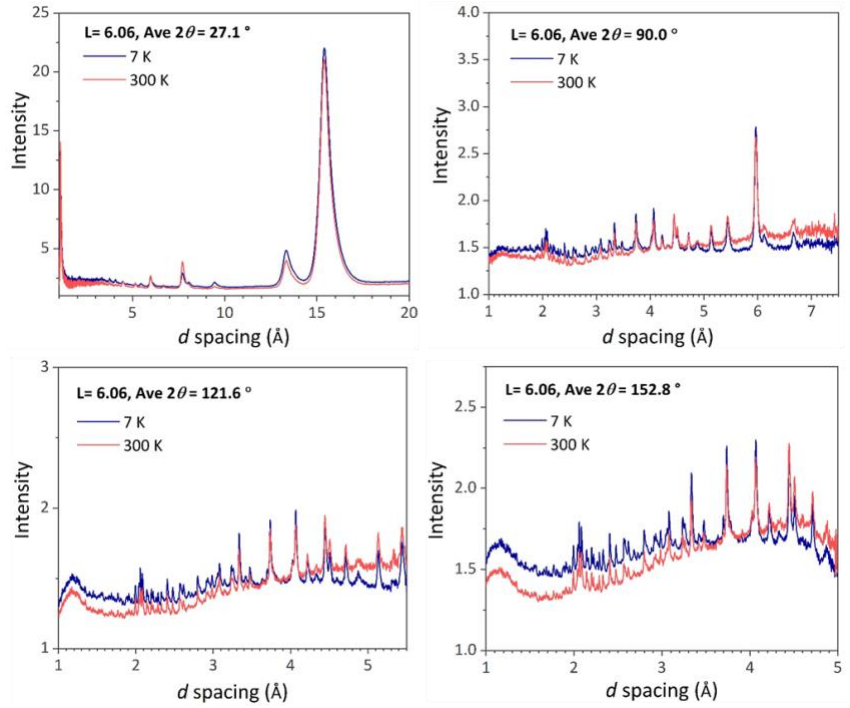

Figure S39 | *In situ* NPD patterns of UiO-bpydc at ND_3 loading (L) of 6.06 mmol/g measured at 7 K (blue line) and 300 K (red line). The data were collected from different detector banks.

It is noted that the change in frameworks structure may occur through linker rotation (like local flexibility in rigid frameworks) which causes the change in peak intensity. Thus, the variation of peak intensities and positions in this study can cause by both orderly adsorbed NH_3 molecules and the linker rotation. One possible way that would help to clarify this observation is to perform the NPD measurement of the ND_3-desorbed samples and see how the diffraction patterns change. As shown by our study, the peak intensities of the extra peaks decreased during ND_3 desorption, we can therefore ensure such additional peaks at high ND_3 loading originated from ND_3 orderly confined in the MOF pores, not from the framework deformation.

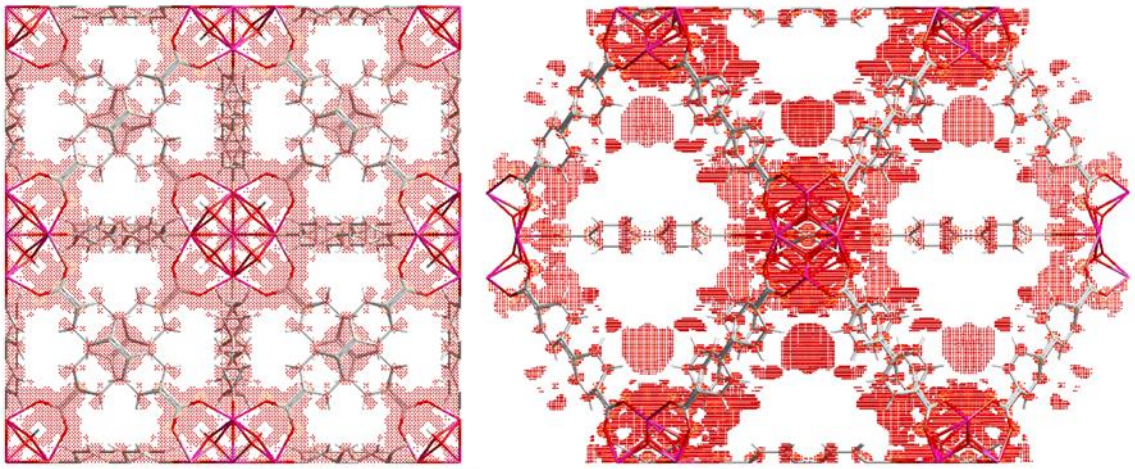

Figure S40 | A Fourier map of ND_3 molecules inside UiO-67 with a loading of 4.63 mmol/g, measured at 7 K.

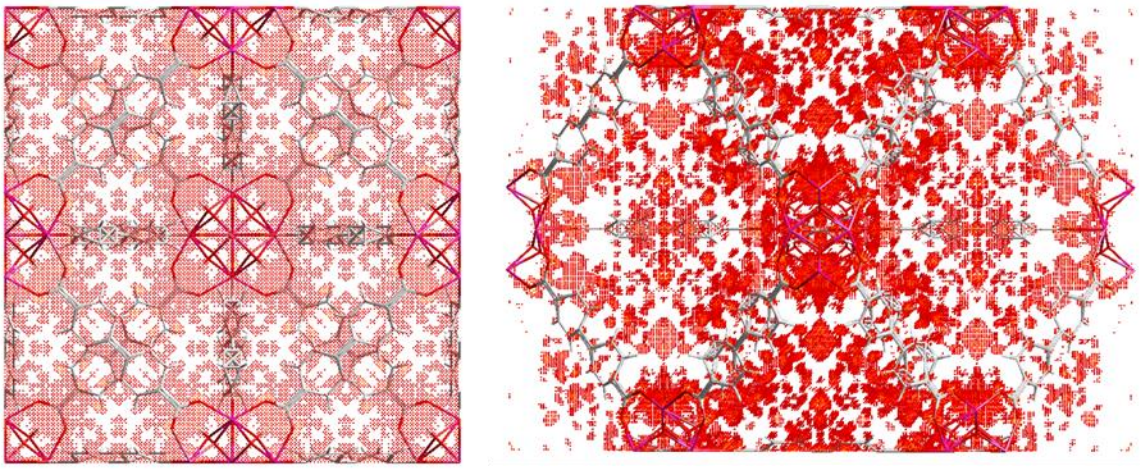

Figure S41 | A Fourier map of ND_3 molecules inside UiO-67 with a loading of 4.63 mmol/g, measured at 300 K.

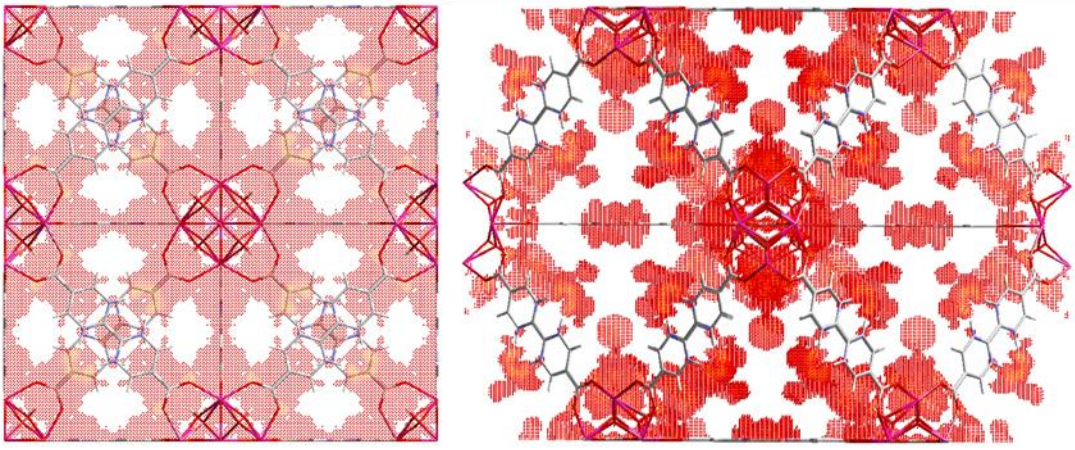

Figure S42 | A Fourier map of ND_3 molecules inside UiO-bpydc with a loading of 4.15 mmol/g, measured at 7 K.

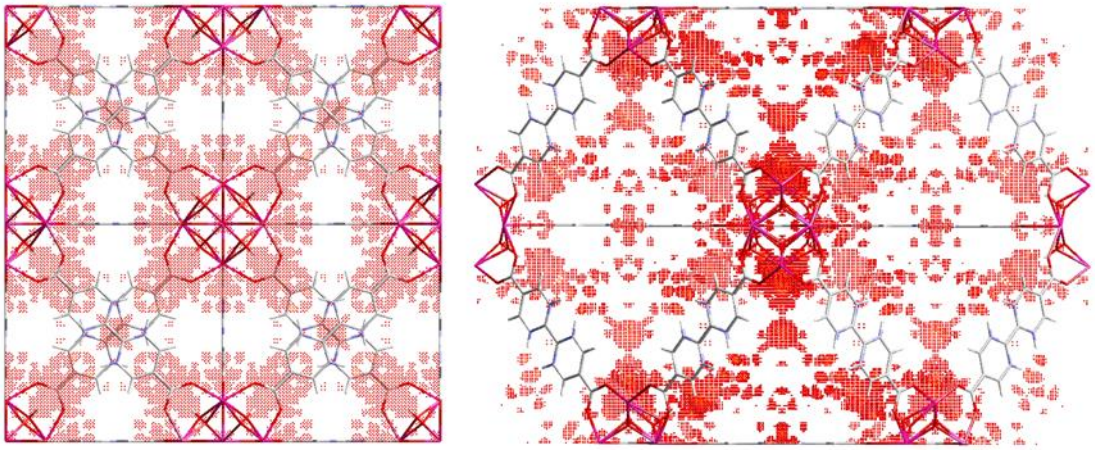

Figure S43 | A Fourier map of ND_3 molecules inside UiO-bpydc with a loading of 4.15 mmol/g, measured at 300 K.

Table S13 | The guiding values of "strong", "moderate" and "weak" hydrogen bonds.[21]

	Strong	Moderate	Weak
Interaction type	Strongly covalent	Mostly electrostatic	Electrostatic/ dispersion
Bond lengths B—H (Å)	1.2- 1.5	ca. 1.0	ca. 1.0
Bond lengths H---A (Å)	1.2- 1.5	1.5- 2.2	> 2.2
Bond lengths B---A (Å)	2.2- 2.5	2.5- 3.2	3.2- 4.0
Bond energy ($kJmol^{-1}$)	63- 167	16- 63	< 16
Bond angles (°)	170- 180	> 130	> 90

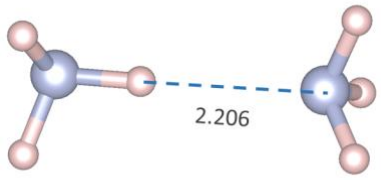

Figure S44 | DFT Optimised structure of NH_3 dimer. The binding energy is 0.13 eV. The unit of the H bond length is in angstrom (Å).

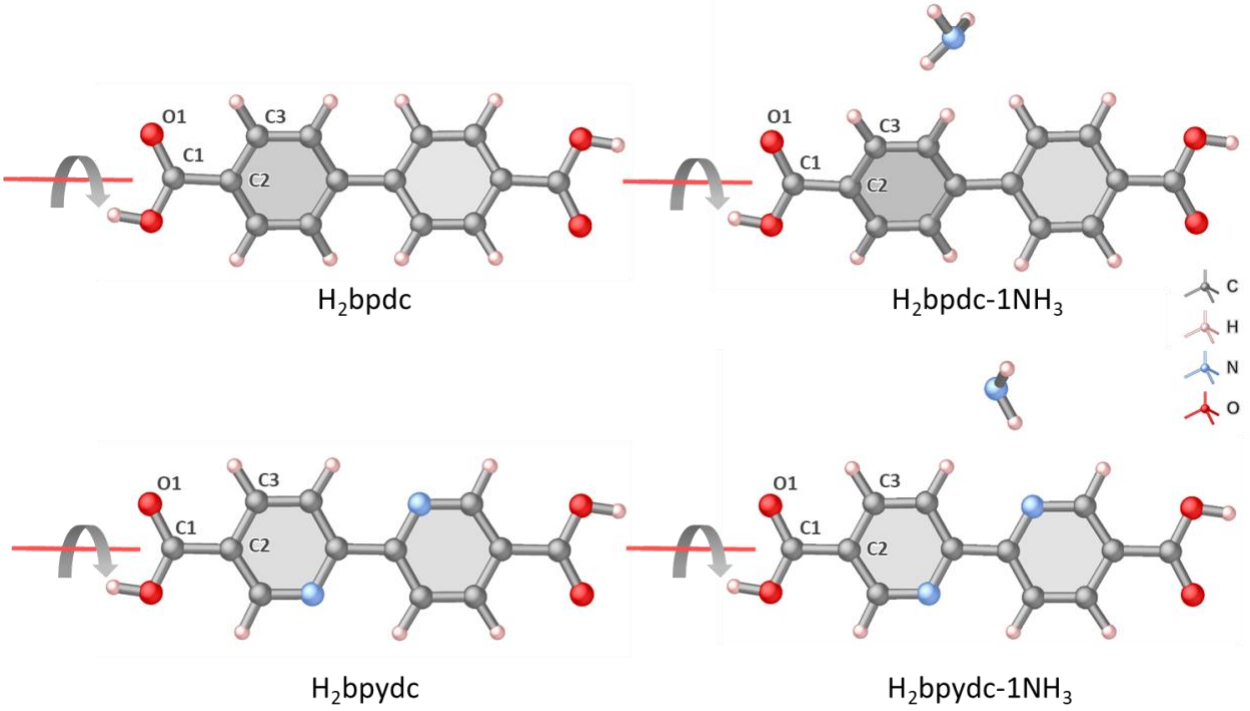

Figure S45 | Proton-capped linker models used for estimating the rotational energy barriers (E_{rb}) of the NH_3-free and NH_3-loaded MOF samples.

Table S14 | Rotational energy barriers (E_{rb}) of the NH_3-free and NH_3-loaded MOF samples estimated from H_2bpdc, H_2bpdc-1NH_3, H_2bpydc, and H_2bpydc-1NH_3 models.

	H_2bpdc	H_2bpdc-1NH_3	H_2bpydc	H_2bppdc-1NH_3
E_{rb} (eV)	0.32	0.33	0.55	0.64
E_{rb} (kJmol^{-1})	30.88	31.84	53.07	61.75

It is known that the modification of the organic linkers with substituent groups and incorporation of guest molecules can change not only the electrostatic effect and equilibrium structure but also the rotational energy barrier (E_{rb}) of the organic linkers in the MOFs.[22] Here, the E_{rb} values of the model MOFs with the abovementioned organic linkers calculated by DFT are shown in Table S16. A potential energy scan was performed to explore the most stable and unstable positions of the organic linkers in the model MOFs during the rotation of the linkers with respect to the dihedral angle γ of O1-C1-C2-C3 (see Figure S45). The derived E_{rb} values were computed as the energy differences between the most unstable and the most stable configurations. The E_{rb} values can indicate the flexibility of the linkers in MOF materials: the higher value of E_{rb}, the less flexibility of the MOF linkers. For the NH_3-free models, it is clearly found that the H_2bpydc linker of UiO-bpydc exhibits higher rotational barrier (0.55 eV or 53.07 kJmol^{-1}) than the H_2bpdc of UiO-67 does (0.32 eV or 30.88 kJmol^{-1}), revealing the less flexibility of the UiO-bpydc due to the

substitution effects. More interestingly, the adsorption of NH_3 in the UiO-bpydc dramatically increases the E_{rb} to 0.64 eV or 61.75 kJmol^{-1}, almost twice higher than that in the UiO-67 analogue. These computational results emphasize the strong influence of NH_3-MOF interactions on controlling the E_{rb} of the MOFs as well as their flexibility towards guest molecules which are in excellent agreement with the corresponding NPD experiments.

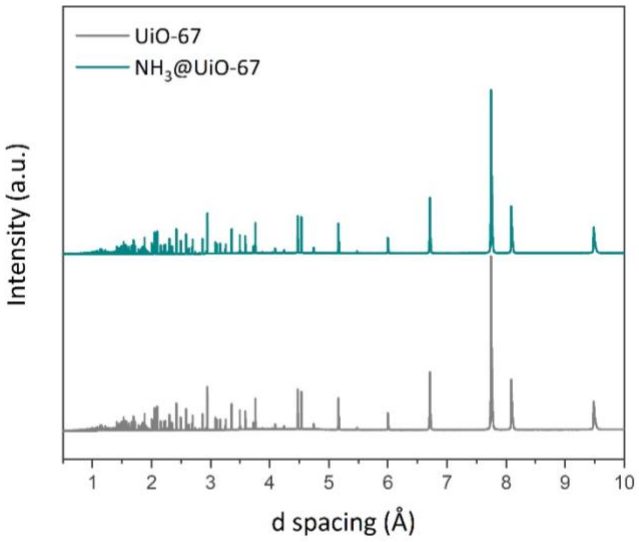

Figure S46 | Synchrotron PXRD patterns of UiO-67 before and after NH_3 adsorption, measured at 298 K.

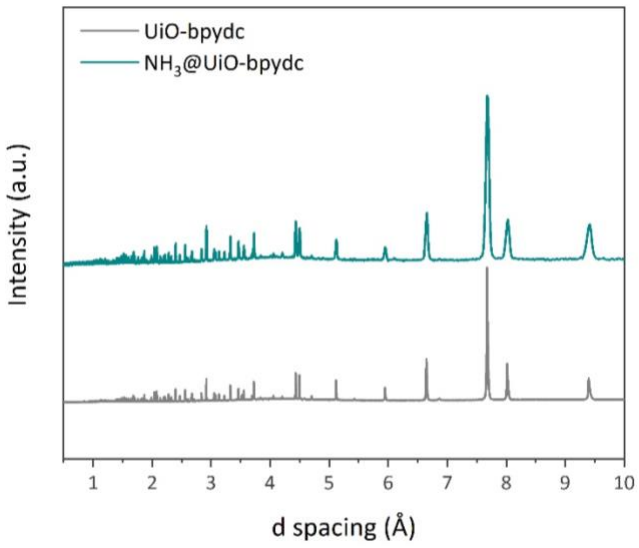

Figure S47 | Synchrotron PXRD patterns of UiO-67 before and after NH_3 adsorption, measured at 298 K.

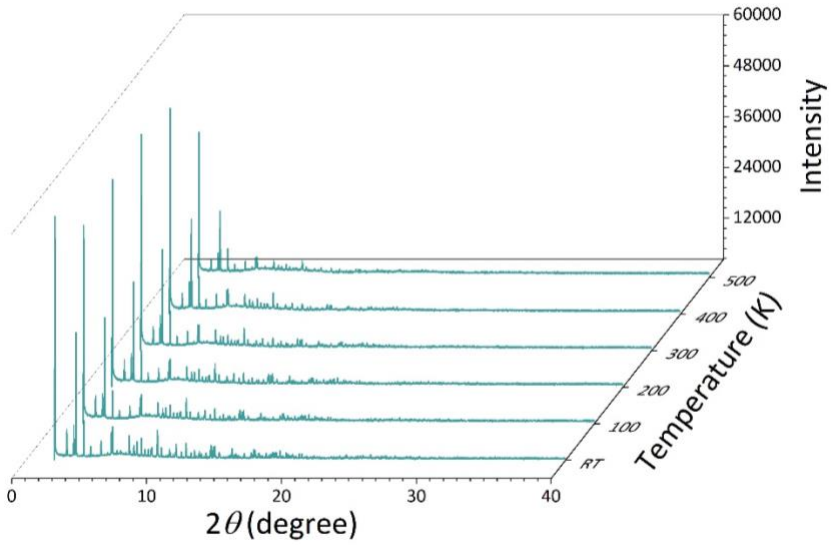

Figure S48 | Synchrotron XRD patterns of the NH_3-loaded UiO-bpydc sample measured at different temperatures from 298 K to 773 K.

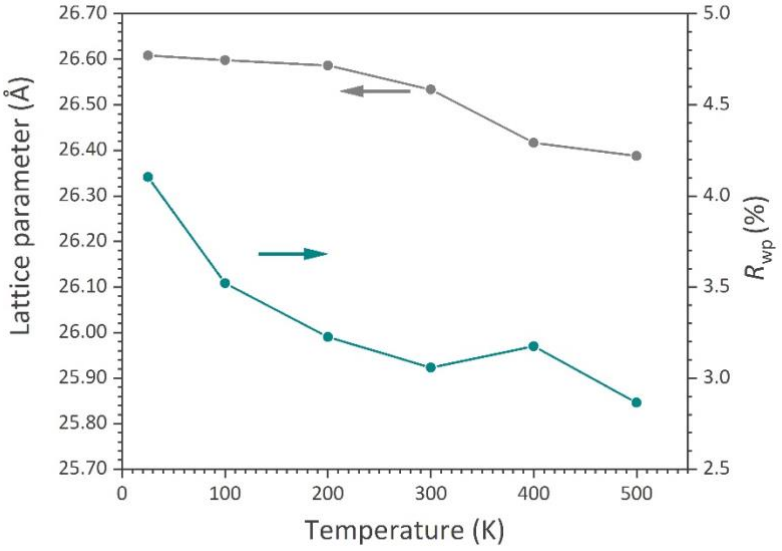

Figure S49 | Refined lattice parameters and their corresponding R_{wp} values of the NH_3-loaded UiO-bpydc sample obtained from the synchrotron XRD results. The maximum standard deviation value of the refined lattice parameters is ± 8.42×10^{-4}.

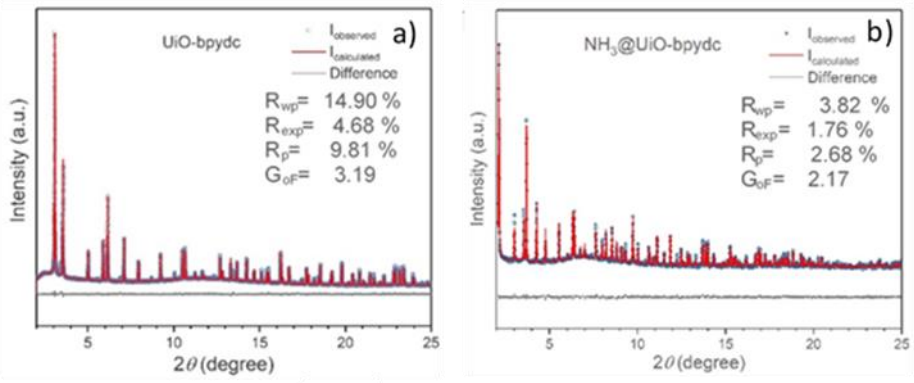

Figure S50 | Synchrotron PXRD patterns and refined NH_3 positions in the channel of the UiO-bpydc structure. (a) Diffraction patterns before and (b) after NH_3 adsorption in UiO-bpydc at 298 K. The ratio of peak intensities alters upon adsorption of NH_3 with a slight peak broadening. The refinement results with acceptable *R*-factors clearly demonstrate the remaining of *Fm*-3*m* space group after NH_3 uptake. The refinement results indicate four possible binding sites of NH_3 in the UiO-bpydc channel. The synchrotron XRD data shows the adsorbed NH_3 are possibly located above the μ_3-O/ or μ_3-OH group (site I, occupancy 0.176 ± 0.007), close to the basal planes of bipyridine linkers (site II, occupancy 0.286 ± 0.014), above the trigonal window with a proximity to site II (site III, occupancy 0.255 ± 0.007) and inside the MOF cavities (site IV, occupancy 0.162 ± 0.005). Note that the NH_3-loaded sample used in the synchrotron PXRD measurement was under saturation. Thus, the quantity of adsorbed NH_3 of this sample is different from that of the sample used in the NPD experiment.

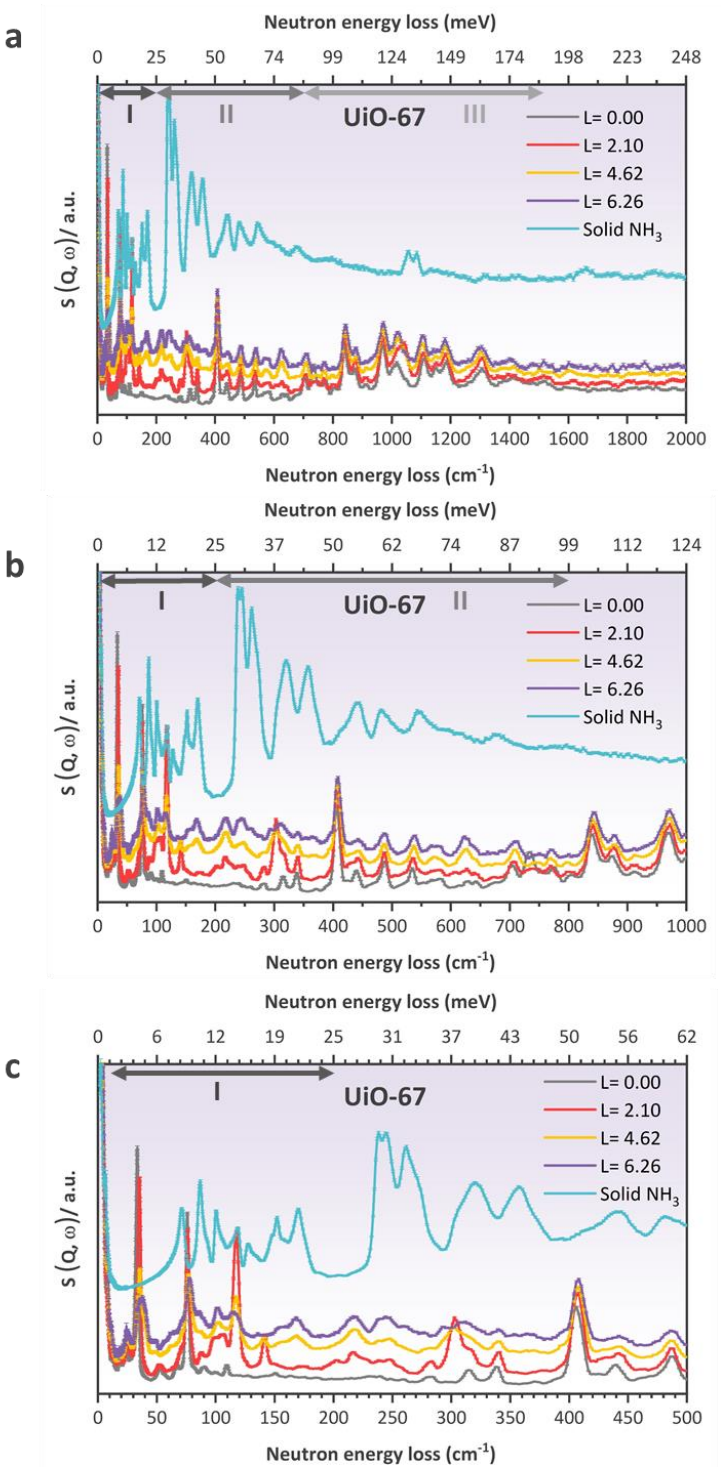

Figure S51 | INS spectra for UiO-67 as a function of NH_3 loadings with the range of neutron energy loss up to 2000 cm^{-1} (248 meV, **a**), 1000 cm^{-1} (124 meV, **b**), and 500 cm^{-1} (62 meV, **c**). The

spectra were collected below 10 K. L refers to loading amount of NH_3 in mmol/g. The INS spectrum of solid NH_3 was provided by the ISIS facility. Note that 1 meV ≈ 8.066 cm^{-1}.

Figure S51 displays the INS spectra up to 2000 cm^{-1} of UiO-67 during NH_3 adsorption measured below 10 K. Considerable changes in the vibrational modes of the NH_3-loaded UiO-67 samples were clearly observed from 20 to 1500 cm^{-1}, suggesting the specific interactions between NH_3 and UiO-67 due to gas adsorption at different binding sites inside the host framework. The origin of the vibrational modes of gas-free UiO-67 was analysed by comparing with the simulated spectrum of UiO-67 obtained from *ab initio* DFT calculations (see Table S17).[23] This can enable a straightforward assignment of the main peaks observed in the INS data. To enable a closer look at the details of the spectra, the vibrational modes are simply divided into three regions; I) below 200 cm^{-1}, II) 200-800 cm^{-1}, and III) 800-1500 cm^{-1}. Region I is associated to deformational and translational motions of Zr clusters and bpdc linkers (lattice vibrations). Region II is assigned to bending and stretching modes of CC aromatic, CH aromatic, COC, Zr-O, and μ_3-OH. Region III corresponded to stretching modes of CC aromatic and COC, as well as collective motions of bpdc linker. Details of the peak assignment are given in Table S17.

Considering the skeletal peaks of UiO-67 in region I, the peak intensities at ca. 31, 52, and 75 cm^{-1} which correspond to libration of the bpdc linkers, deformation of Zr polyhedra, and rotation of the bpdc linkers sharply decreased together with a slight blue shift during the progressive NH_3 adsorption. This result is much likely due to a suppression and stiffening of lattice motions such as linker rotation resulting from either a host-guest interaction or guest-induced gate opening as previously reported in the literature.[24] In region II (200-800 cm^{-1}), we observed substantial changes in peak positions to higher energy transfer over the whole range, except a minor red shift found at ca. 480 and 775 cm^{-1}. The most notable decrease in peak intensity was detected at ca. 740 cm^{-1}. This peak is assigned to bending modes of μ_3-OH and CH aromatic, suggesting the hindrance of these motions when interact with NH_3 molecules. At higher vibrational frequencies (region III), we observed a combination of blue shift (820-1000 cm^{-1}), associated to bending modes of μ_3-OH and CH aromatic and red shift (1050-1350 cm^{-1}), correlated to collective modes of bpdc and stretching modes of CC aromatic with increased NH_3 uptake. These phenomena reflect the engagement of the host to form H-bond and supramolecular interactions with the adsorbed NH_3, in well agreement with the NPD and DFT study.

The experimental INS spectrum of solid NH_3 provided by the ISIS facility was plotted against the spectra of NH_3-loaded UiO-67 samples (Supplementary Figure 51). With increasing NH_3, additional well-defined peaks were clearly observed in the energy transfer range of 60 and 1100 cm^{-1}. Although these peaks emerged at significantly lower frequencies, their overall characteristics were similar to the vibrational spectrum of solid NH_3, indicating the incorporation of NH_3 inside UiO-67. The peaks appeared at low energy transfer (60-150 cm^{-1}) can be ascribed to translational modes, whereas ones located around 150-350 cm^{-1} can be attributed to librational motions of NH_3.[25] Comparing among the NH_3-loaded samples, distinct changes in peak intensities and positions associated to NH_3 were detected. These alterations suggest that the NH_3 molecules experience different environment inside the pores of UiO-67, forming either NH_3-framework or NH_3-NH_3 interactions. For a deeper discussion on types of interactions, we are currently performing DFT calculations to extract vibrational modes of the loaded samples and simulate their

corresponding INS spectra. Comparison between the observed and simulated INS spectra of the ammoniated MOF samples will be discussed and reported in the near future.

Table S15 | Calculated and experimental vibrational modes of gas-free UiO-67. The experiment data were recorded below 10 K by using an INS technique.

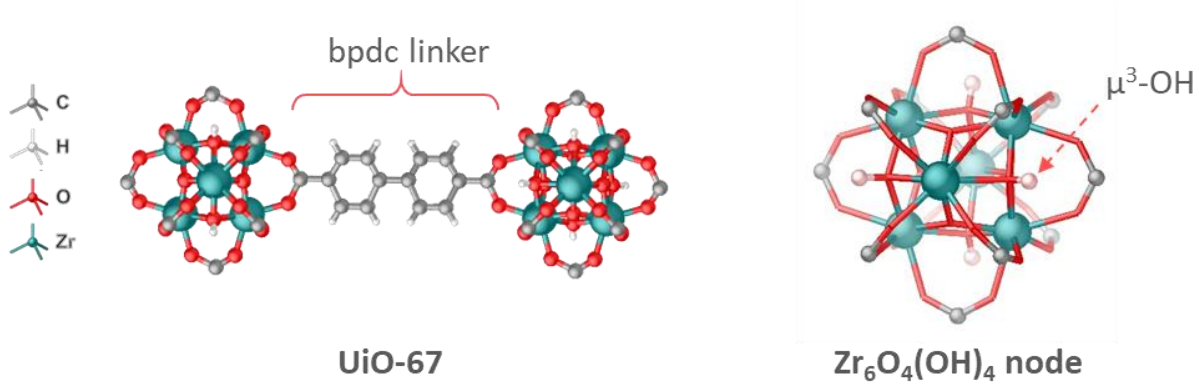

Frequency (cm^{-1})		Band assignment
Calculated from ref[23]*	**Experimental**	
26, 31	22, 26	Linker libration
35, 37	43	Linker rotation
45, 47	63, 73	PH libration+ Linker rocking+ Linker rotation
70	77	Linker rocking+ PH deformation
80, 81		Linker rotation
90, 92, 93	90	Linker wagging+ Linker rocking+ PH deformation
109	108	Linker wagging+ Linker twisting+ PH deformation
124	117	Linker stretching+ Linker rocking, PH deformation
174, 176	178	Linker wagging+ Linker rocking+ PH deformation
190	194	Linker wagging+ PH deformation
204, 210, 212	206	OCO twisting+ Linker rocking (non-rigid)+ PH deformation
221, 224	228	OCO twisting+ Linker wagging+ Linker rocking+ PH deformation+ OH bending
236, 241	235	OH bending+ Linker wagging+ PH deformation
248, 250	247	Linker wagging+ OH stretching+ OCO twisting+ PH deformation

Frequency (cm^{-1})		Band assignment
Calculated from ref[23]*	**Experimental**	
287, 291	288	PH stretching (breathing)+ Linker stretching (rigid)+ Linker rocking (non-rigid)+ Linker wagging+ OCO bending
305	306	PH stretching (breathing)+ Linker stretching (rigid)
318, 323	321	OCO bending+ PH deformation+ Linker rocking (non-rigid)+ Linker wagging
349	339	Linker wagging (non-rigid)+ PH deformation
375	376	Linker wagging (non-rigid)+ Linker rocking (non-rigid)
381	n.o.	Zr-OCO stretching+ PH deformation+ Linker stretching (rigid)
395, 402	397	Zr- μ_3-O and Zr-μ_3-OH stretching+ PH deformation
419-421	412	Zr- μ_3-O and Zr-μ_3-OH bending+ PH deformation+ Linker rocking (non-rigid)
435	435	CC_{ring} deformation (OP+ IP) + Zr-OCO deformation+ Zr- μ_3-O and Zr-μ_3-OH bending
457	458	Zr-μ_3-OH bending+ Zr- μ_3-O stretching+ OCO bending (IP)
486	486	Zr- μ_3-O stretching+ PH deformation
-	536	Zr-OCO stretching+ Zr- μ_3-O and Zr-μ_3-OH bending+ $CC_{backbone}$ stretching
552	n.o.	Zr-OCO stretching+ CC_{ring} deformation (OP)+ Zr-μ_3-OH bending
570, 571, 574	575	Zr- μ_3-O and Zr-μ_3-OH deformation+ CC_{ring} and CH_{ring} deformation (IP)+ Zr-OCO stretching
-	621	CC_{ring} deformation (IP)
642, 643	634	CC_{ring} and CH_{ring} deformation (IP)
657, 670	665	Zr-O deformation+ CC_{ring} and CH_{ring} deformation (IP)
686, 694	695	OH bending+ OCO bending+ CC_{ring} deformation (IP)
717, 720, 723	723	OH bending+ OCO bending+ CC_{ring} deformation (OP, rigid)+ CH_{ring} wagging (rigid)
730	733	OH bending+ OCO bending+ CC_{ring} deformation (OP, rigid)+ CH_{ring} wagging (rigid)

Frequency (cm^{-1})		Band assignment
Calculated from ref[23]*	**Experimental**	
763	763	OCO bending+ CC_{ring} bending and stretching (IP)
776, 777	784	OH bending+ OCO bending+ CH_{ring} deformation (OP)
819	n.o.	CH_{ring} wagging+ CC_{ring} deformation (OP)
-	836	CH_{ring} wagging
868, 870	871	CH_{ring} wagging+ OCO bending+ OH bending
-	969	CH_{ring} twisting
1022	1020	CH_{ring} stretching+ CC_{ring} deformation (IP)
1051	1047	CH_{ring} rocking+ CC_{ring} deformation (IP)
-	1112	CH_{ring} scissoring+ CC_{ring} deformation (IP)
1140, 1141, 1145	1146	CH_{ring} scissoring
1173, 1175, 1176	1180	CH_{ring} close to Zr node bending+ CC_{ring} deformation (IP)
1210	n.o.	Collective mode of the BPDC linker
1309	1304	CH_{ring} rocking+ CC_{ring} deformation (IP)
1352	n.o.	CH_{ring} rocking+ CC_{ring} deformation (IP)
1422	n.o.	OCO sym. Stretching
1538	n.o.	CH_{ring} rocking+ CC_{ring} deformation (IP)
1630	n.o.	OCO asym. Stretching+ CC_{ring} deformation (IP)
1667	n.o.	CH_{ring} scissoring+ CC_{ring} deformation (IP)

n.o. = not observed; IP= in plane; OP= out of plane; PH= Zr-O polyhedral; sym= symmetric; asym.= asymmetric.

* The data were performed at hybrid B3LYP level of calculations and the obtained structure was optimised in *F*23 space group.

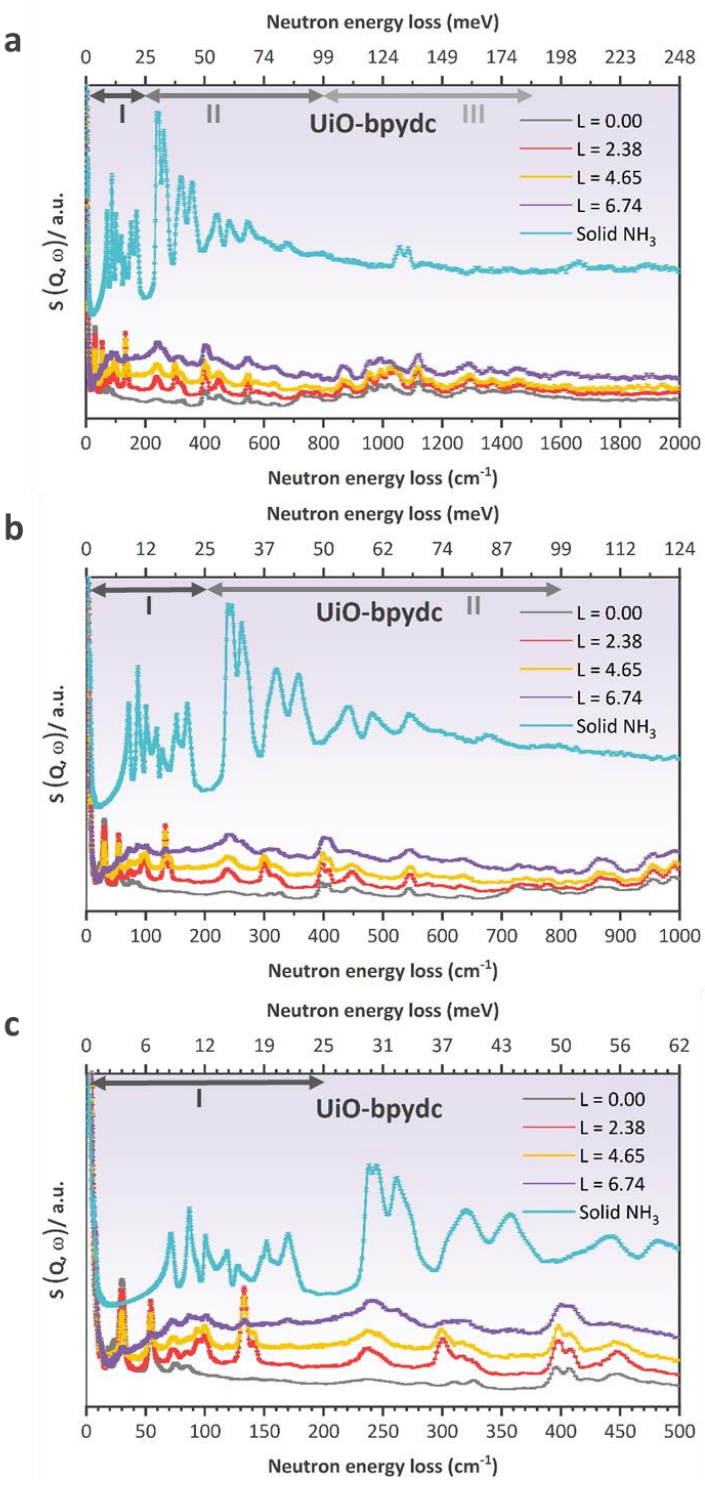

Figure S52 | INS spectra for UiO-bpydc as a function of NH_3 loadings with the range of neutron energy loss up to 2000 cm^{-1} (248 meV, a), 1000 cm^{-1} (124 meV, b), and 500 cm^{-1} (62 meV, c). The spectra were collected below 10 K. L refers to loading amount of NH_3 in mmol/g. The INS spectrum of solid NH_3 was provided by the ISIS. Note that 1 meV ≈ 8.066 cm^{-1}.

Considering the skeletal peaks of UiO-bpydc in region I, the peak intensities at ca. 30 and 55 cm^{-1} which possibly correspond to rotational modes of the bpydc linkers sharply decreased together with a slight blue shift during the progressive NH_3 adsorption. These peaks almost disappear at the highest loading of NH_3 (purple line). This result is much likely due to a suppression and stiffening of lattice motions such as linker rotation due to a strong host-guest interaction. It is also worth noting that the decline of peak intensities of UiO-bpydc was more prominent than those of UiO-67 (Figure S51), implying a relatively stronger host-guest interaction due to H-bonding between NH_3 and bipyridine linkers.

Table S16 | Comparison of the total occupancies of the adsorbed ND_3 in UiO-67-type MOFs at different temperatures obtained from Rietveld refinement of NPD data.

Sample	Measurement Temperature (K)	Total ND_3 occupancies from the Rietveld refinement (molecule per asymmetric unit)		
		1st loading	2nd loading	3rd loading
UiO-67	300	0.03	0.10	0.32
	7	0.03	0.11	0.32*
UiO-bpydc	300	0.11	0.12	0.26
	7	0.11	0.12	0.27

3. Further research

Ongoing efforts are focused on using neutron scattering techniques combined with computational modelling to establish the dynamic behaviors and kinetics of this system and support the H-bonding network model.

4. References

1. Cavka, J. H.; Jakobsen, S.; Olsbye, U.; Guillou, N.; Lamberti, C.; Bordiga, S.; Lillerud, K. P., A New Zirconium Inorganic Building Brick Forming Metal Organic Frameworks with Exceptional Stability. *J. Am. Chem. Soc.* **2008,** *130* (42), 13850-13851.

2. Gutov, O. V.; Hevia, M. G.; Escudero-Adán, E. C.; Shafir, A., Metal–Organic Framework (MOF) Defects under Control: Insights into the Missing Linker Sites and Their Implication in the Reactivity of Zirconium-Based Frameworks. *Inorg. Chem.* **2015,** *54* (17), 8396-8400.

3. Chapon, L. C.; Manuel, P.; Radaelli, P. G.; Benson, C.; Perrott, L.; Ansell, S.; Rhodes, N. J.; Raspino, D.; Duxbury, D.; Spill, E.; Norris, J., Wish: The New Powder and Single Crystal Magnetic Diffractometer on the Second Target Station. *Neutron News* **2011,** *22* (2), 22-25.

4. Zhao, P.; Fang, H.; Mukhopadhyay, S.; Li, A.; Rudić, S.; McPherson, I. J.; Tang, C. C.; Fairen-Jimenez, D.; Tsang, S. C. E.; Redfern, S. A. T., Structural Dynamics of a Metal–Organic Framework Induced by CO_2 Migration in Its Non-Uniform Porous Structure. *Nat. Commun.* **2019,** *10* (1), 999.

5. Wang, B.; Huang, H.; Lv, X.-L.; Xie, Y.; Li, M.; Li, J.-R., Tuning CO_2 Selective Adsorption over N_2 and CH_4 in UiO-67 Analogues through Ligand Functionalization. *Inorg. Chem.* **2014,** *53* (17), 9254-9259.

6. Yang, S.; Sun, J.; Ramirez-Cuesta, A. J.; Callear, S. K.; David, W. I. F.; Anderson, D. P.; Newby, R.; Blake, A. J.; Parker, J. E.; Tang, C. C.; Schröder, M., Selectivity and Direct Visualization of Carbon Dioxide and Sulfur Dioxide in a Decorated Porous Host. *Nat. Chem.* **2012**, *4*, 887.

7. Yang, S.; Ramirez-Cuesta, A. J.; Newby, R.; Garcia-Sakai, V.; Manuel, P.; Callear, S. K.; Campbell, S. I.; Tang, C. C.; Schröder, M., Supramolecular Binding and Separation of Hydrocarbons within a Functionalized Porous Metal–Organic Framework. *Nat. Chem.* **2015**, *7* (2), 121-129.

8. Lu, Z.; Godfrey, H. G. W.; da Silva, I.; Cheng, Y.; Savage, M.; Tuna, F.; McInnes, E. J. L.; Teat, S. J.; Gagnon, K. J.; Frogley, M. D.; Manuel, P.; Rudić, S.; Ramirez-Cuesta, A. J.; Easun, T. L.; Yang, S.; Schröder, M., Modulating Supramolecular Binding of Carbon Dioxide in a Redox-Active Porous Metal-Organic Framework. *Nat. Commun*. **2017**, *8* (1), 14212.

9. Thompson, S. P.; Parker, J. E.; Potter, J.; Hill, T. P.; Birt, A.; Cobb, T. M.; Yuan, F.; Tang, C. C., Beamline I11 at Diamond: A New Instrument for High Resolution Powder Diffraction. *Rev. Sci. Instrum.* **2009,** *80* (7), 075107.

10. Pinna, R. S.; Zanetti, M.; Rudić, S.; Parker, S. F.; Armstrong, J.; Waller, S. P.; Zacek, D.; Smith, C.; Harrison, S. M.; Gorini, G.; Fernandez-Alonso, F., The TOSCA Spectrometer at ISIS: the Guide Upgrade and Beyond. *Journal of Physics: Conference Series* **2018,** *1021*, 012029.

11. Arnold, O.; Bilheux, J. C.; Borreguero, J. M.; Buts, A.; Campbell, S. I.; Chapon, L.; Doucet, M.; Draper, N.; Ferraz Leal, R.; Gigg, M. A.; Lynch, V. E.; Markvardsen, A.; Mikkelson, D. J.; Mikkelson, R. L.; Miller, R.; Palmen, K.; Parker, P.; Passos, G.; Perring, T. G.; Peterson, P. F.; Ren, S.; Reuter, M. A.; Savici, A. T.; Taylor, J. W.; Taylor, R. J.; Tolchenov, R.; Zhou, W.; Zikovsky, J., Mantid—Data Analysis and Visualization Package for Neutron Scattering and μ SR Experiments. *Nucl. Instrum. Methods. Phys. Res. B* **2014,** *764*, 156-166.

12. Coelho, A., TOPAS and TOPAS-Academic: an Optimization Program Integrating Computer Algebra and Crystallographic Objects Written in C++. *J. Appl. Crystallogr.* **2018,** *51* (1), 210-218.

13. Ko, N.; Hong, J.; Sung, S.; Cordova, K. E.; Park, H. J.; Yang, J. K.; Kim, J., A Significant Enhancement of Water Vapour Uptake at Low Pressure by Amine-Functionalization of UiO-67. *Dalton Trans.* **2015,** *44* (5), 2047-2051.

14. Gonzalez, M. I.; Bloch, E. D.; Mason, J. A.; Teat, S. J.; Long, J. R., Single-Crystal-to-Single-Crystal Metalation of a Metal–Organic Framework: A Route toward Structurally Well-Defined Catalysts. *Inorg. Chem.* **2015,** *54* (6), 2995-3005.

15. Blöchl, P. E., Projector Augmented-Wave Method. *Phys. Rev. B* **1994,** *50* (24), 17953-17979.

16. Grimme, S.; Antony, J.; Ehrlich, S.; Krieg, H., A Consistent and Accurate Ab Initio Parametrization of Density Functional Dispersion Correction (DFT-D) for the 94 Elements H-Pu. *J. Chem. Phys.* **2010,** *132* (15), 154104.

17. Zhao, Y.; Truhlar, D. G., The M06 Suite of Density Functionals for Main Group Thermochemistry, Thermochemical Kinetics, Noncovalent Interactions, Excited States, and Transition Elements: Two New Functionals and Systematic Testing of Four M06-Class Functionals and 12 Other Functionals. *Theor. Chem. Acc.* **2008,** *120* (1), 215-241.

18. Weigend, F.; Ahlrichs, R., Balanced Basis Sets of Split Valence, Triple Zeta Valence and Quadruple Zeta Valence Quality for H to Rn: Design and Assessment of Accuracy. *Phys. Chem. Chem. Phys.* **2005,** *7* (18), 3297-3305.

19. Weigend, F., Accurate Coulomb-Fitting Basis Sets for H to Rn. *Phys. Chem. Chem. Phys.* **2006,** *8* (9), 1057-1065.

20. Frisch, M. J.; Trucks, G. W.; Schlegel, H. B.; Scuseria, G. E.; Robb, M. A.; Cheeseman, J. R.; Scalmani, G.; Barone, V.; Petersson, G. A.; Nakatsuji, H.; Li, X.; Caricato, M.; Marenich, A. V.; Bloino, J.; Janesko, B. G.; Gomperts, R.; Mennucci, B.; Hratchian, H. P.; Ortiz, J. V.; Izmaylov, A. F.; Sonnenberg, J. L.; Williams; Ding, F.; Lipparini, F.; Egidi, F.; Goings, J.; Peng, B.; Petrone, A.; Henderson, T.; Ranasinghe, D.; Zakrzewski, V. G.; Gao, J.; Rega, N.; Zheng, G.; Liang, W.; Hada, M.; Ehara, M.; Toyota, K.; Fukuda, R.; Hasegawa, J.; Ishida, M.; Nakajima, T.; Honda, Y.; Kitao, O.; Nakai, H.; Vreven, T.; Throssell, K.; Montgomery Jr., J. A.; Peralta, J. E.; Ogliaro, F.; Bearpark, M. J.; Heyd, J. J.; Brothers, E. N.; Kudin, K. N.; Staroverov, V. N.; Keith, T. A.; Kobayashi, R.; Normand, J.; Raghavachari, K.; Rendell, A. P.; Burant, J. C.; Iyengar, S. S.; Tomasi, J.; Cossi, M.; Millam, J. M.; Klene, M.; Adamo, C.; Cammi, R.; Ochterski, J. W.; Martin, R. L.; Morokuma, K.; Farkas, O.; Foresman, J. B.; Fox, D. J. *Gaussian 16 Rev. C.01*, Wallingford, CT, 2016.

21. Steiner, T., The Hydrogen Bond in the Solid State. *Angew. Chem. Int. Ed.* **2002,** *41* (1), 48-76.

22. Gonzalez-Nelson, A.; Coudert, F.-X.; van der Veen, M. A., Rotational Dynamics of Linkers in Metal–Organic Frameworks. *Nanomaterials* **2019,** *9* (3).

23. Chavan, S.; Vitillo, J. G.; Gianolio, D.; Zavorotynska, O.; Civalleri, B.; Jakobsen, S.; Nilsen, M. H.; Valenzano, L.; Lamberti, C.; Lillerud, K. P.; Bordiga, S., H_2 Storage in Isostructural UiO-67 and UiO-66 MOFs. *Phys. Chem. Chem. Phys.* **2012,** *14* (5), 1614-1626.

24. Easun, T. L.; Moreau, F.; Yan, Y.; Yang, S.; Schröder, M., Structural and Dynamic Studies of Substrate Binding in Porous Metal–Organic Frameworks. *Chem. Soc. Rev.* **2017,** *46* (1), 239-274.

25. Binbrek, O. S.; Anderson, A., Raman Spectra of Molecular Crystals. Ammonia and 3-deutero-Ammonia. *Chem. Phys. Lett.* **1972,** *15* (3), 421-427.